Politecnico di Milano
School of Industrial and Information Engineering
Master degree in Engineering Physics
Department of Physics

First-principle investigation of Kohn anomalies and Peierls transitions in metallic nanowires

Promoter: Prof. Marco Finazzi

Author: Enrico Marazzi 920909

Anno Accademico 2020-2021

Contents

List of Figures

List of Tables

Abstract

In this thesis, a theoretical analysis of the causes and effects of charge density waves (CDW) in metals is presented, focusing on 1D systems. CDWs are the periodic spatial modulation of the charge density that occurs in some metals at T = 0 K. The origin of CDWs varies depending on the dimensionality of the metal itself. In 1D, it is mainly due to the Fermi surface nesting, while in 2D and 3D, the origin ought to be found in the electron-phonon coupling, which anyway plays a role in 1D systems as well. Furthermore, CDWs induce instabilities in the lattice too. As mentioned, the ions might redistribute following different processes. Firstly, a Peierls transition may take place: the unit cell dimension doubles, the number of atoms in it doubles as well, and a metal-insulator transition occurs. The transition is energetically favored when the reduction in energy due to the opening of the gap overcomes the energy needed for the lattice relaxation. Secondly, a Kohn instability might appear: a phonon mode softens due to the lack of screening ability of the electron gas for a certain wave vector. A lower temperature enhances the depth of the dip. When the phonon frequency becomes negative, the mode is unstable and a structural relaxation takes place. A metal-insulator transition is not guaranteed by this latter structural relaxation. Afterwards, a first-principle analysis is performed using the ABINIT software. The analysis is organized as follows: the electron band structure is computed as well as the phonon dispersion relation. Comparing the two, the occurrences of Kohn anomalies and their relation with the Fermi surface nesting is portrayed. Afterwards, electron-phonon coupling matrix elements are calculated and related to the properties of the Kohn anomalies.

Introduction

The concept of charge density waves (CDW) is present in the scientific literature since 1950s [1] and the first suggestion that metallic systems at low temperatures are not stable dates back to the 1930s [2]. CDWs have first been observed in one-dimensional (1D) structures. Then, proofs of the appearance of CDWs in two- (2D) and three-dimensional (3D) materials have been reported as well [3,4]. Nonetheless, since almost a century, this is an open question, it is still discussed. A great deal of work is still carried out both on theoretical and experimental sides in order to get a full understanding of the problem [5].

A first issue is the origin of charge density waves in metals which varies depending on the material and on its dimensionality. As we shall see, the CDWs appear in 1D materials because of an instability of the Fermi surface, while in 2D and 3D materials the origin lies in the electron-phonon interaction. Moreover, the consequences of the formation of charge density waves are quite different: firstly, metal-insulator Peierls transition might take place under certain conditions. Secondly, softenings of the phonon modes can occur leading to a structural relaxation. However, structural relaxations might take place without a metal-insulator transition.

At the state-of-the-art, CDWs are known to occur in several systems. Starting from 1D, nanowires have been widely studied, since they were the first systems in which CDWs were observed. Particularly interesting structures are the polymeric metallic chains such as polyacetylene or TTF-TCNQ (tetrathiafulvalene-tetracyano-quinodimethane). On the one hand, while remaining a relatively simple system, polyacetylene has the advantage of being a real system, differently from the ones that will be studied in this work, and a Peierls instability is well-known to occur, making this system a good proof of the principles. On the other hand, TTF-TCNQ is a quasi-1D system which, however, shows all the properties of a perfect 1D system, i.e. Fermi surface nesting, peak in the Lindhard response function, Kohn anomaly and metal-insulator transition [6]. Other 1D structures now known to show CDWs are transitional

metal trichalcogenides, such as $NbSe_3$. Passing to 2D structures, particular interest is given to transition metal dichalcogenide, e.g. $NbSe_2$, and cuprates. The relationship between CDW and superconductivity has emerged since the discovery of unconventional superconductivity in cuprates. These are often considered as layered quasi-2D materials and the competition between charge ordering a superconductivity attracts a large deal of study, especially in $YBa_2Cu_3O_{6+x}$ (YBCO) [6]. This might become an important field of study in the next future.

This thesis is devoted to the analyzes of the appearance of CDW in metallic structures, with a particular focus on nanowires, and a brief mention of 3D systems. The aim is to explore the properties of CDWs in 1D systems and then to apply the acquired knowledge to bulk materials. This is done because one-dimensional systems show CDWs in their simplest way. Moreover, it is easier to perform an analysis in a single direction, while the situation gets much more complicated approaching two- and three-dimensional materials.

On the one hand, in chapter 1, a theoretical overview of the problem is provided. The possible origins of CDWs in metallic nanowires are exposed, i.e. the Fermi surface nesting that leads to the divergence of the Lindhard response function and the electron-phonon coupling. Furthermore, the possible consequences, i.e. the Peierls transition and Kohn anomalies, are presented. As it will be detailed in the chapter, the former is the metal-insulator transition that follows from a structural relaxation; the latter is the softening of a phonon mode due to the lack of conductive electrons' screening ability at a particular wave vector. On the other hand, in chapter 2, the first principle analysis of metallic systems is introduced. The studied systems are silicon and aluminium nanowires. These fictitious systems, which are not found in nature, are studied in order to get a better comprehension of the physical phenomena. Indeed, it will be explained how the silicon linear chain is unstable and a more stable system is the zigzag. The dispersion relation of both the linear and zigzag chains are calculated and the occurrences of Kohn anomaly analyzed. In order to do that, various physical quantities such as electron and phonon band structures, electron-phonon coupling matrix elements and the first order perturbation of potential are computed. Afterwards, the bulk systems are explored as well.

Possible future developments are finding a systematic way to treat linear chains, which means predicting the properties of phonon band structures without actually calculating or measuring them. Then, it will be needed to expand the treatment to real systems, starting from the ones

whose properties are known, e.g. polyacetylene and TTF-TCNQ. Afterwards, the work may be repeated for 2D and 3D materials and a general way to treat metals can be achieved. As it will be shortly discuss in the next chapters, the identification of CDWs' location is much more complicated in 2D and 3D materials since the shape of the Fermi surface is more complex; a detailed study is therefore needed.

The ab initio calculations are performed using ABINIT [7–12]. ABINIT is a software suite used to calculate the optical, mechanical, vibrational properties of molecules, nanostructures and solids with any chemical compositions. It relies on density functional theory and density functional perturbation theory. Together with ABINIT, ABIPY [13], a PYTHON library, is used to analyse the results.

Chapter 1

Theoretical background

1.1 Charge density waves

In metals, the charge density is highly uniform and the ions in their equilibrium positions form a perfectly periodic lattice (cfr. figure 1.1). However, in some metals at $T = 0\ K$, the Fermi surface associated to such a lattice becomes unstable and the charge redistributes forming a periodic spatial modulation [6]. This modulation of the electron density is called charge density wave (CDW). The modulated charge can be expressed as [1]

$$\rho(\vec{r}) = \rho_0 + \rho_1 \cos\left(2\vec{k}_F \cdot \vec{r} + \varphi\right) \tag{1.1}$$

where ρ_0 is the unperturbed electron density of the metal, $\vec{k}_F$ is the Fermi wave vector, and φ is the phase of the condensate.

Even though the appearance of CDWs in metals may have different origins depending on the system, i.e. the type of metal and the dimensionality (1D, 2D or 3D), CDWs have some common traits. Indeed, they modify the ionic potential and, therefore, lead to new equilibrium positions for the atoms in the lattice. Moreover, they are characterized by a transition temperature (T_{CDW}) above which the charge density of

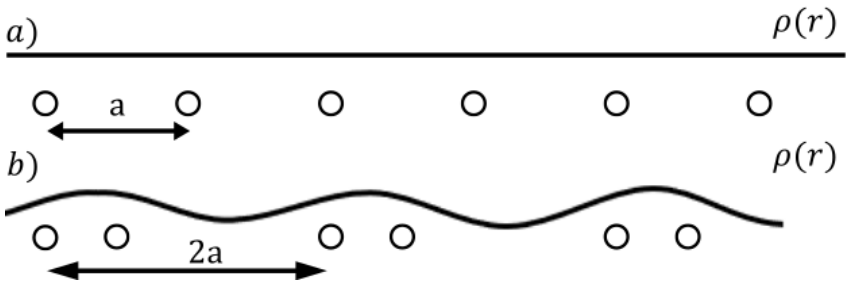

Figure 1.1: Electron density and periodic lattice without (a) and with (b) the formation of charge density waves. Inspired by Ref. [1]

the system is again uniform. The most straightforward CDW occurrence, that was also the first to be observed, is the instability of a one-dimensional chain of equally-spaced atoms. This was pointed out by Peierls in 1930 [2]. Another consequence of charge density waves is the Kohn anomaly [14]. These two topics will be explored in more details in sections 1.4 and 1.5, respectively.

CDWs may also emerge in two-dimensional systems, e.g. $NbSe_2$, which shows a Kohn-like anomaly. However, the origin has nothing to do with Peierls's picture [15]. It actually has to be ascribed to the electron-phonon coupling. Three-dimensional systems show CDWs as well. Nonetheless, the situation is even more complicated and it is not easy to isolate a single charge density wave [6].

Since CDWs arise in their simplest form in one-dimensional structures [16], the main focus of this work will be on this type of systems and their properties, in particular on metallic one-dimensional (1D) structures or metallic nanowires (NW). Therefore, section 1.2 will present a summary of the electronic properties of one-dimensional structures: the electronic dispersion relation and the geometry of the Fermi surface. Consequently, in section 1.3, the Lindhard response function and its impact on electronic charge stability is explored: the origin of the electronic instability that leads to the charge density wave is discussed. Subsequently, as already mentioned, in sections 1.4 and 1.5, Peierls transitions and Kohn anomalies are detailed. Then, in section 1.6, the electron-phonon coupling, i.e. the other key element for the emergence of the transition, is introduced. Finally, in section 1.7, some important final remarks are made: in particular, what happens when the Fermi surface consists of more than one point.

1.2 One-dimensional structures

The solids that populate our world are characterized by finite dimensions in the three spatial dimensions. Nanoscience deals with materials that are characterized by, at least, one dimension that is in the nanometer (nm) range. Therefore, two-dimensional (2D), one-dimensional (1D) and zero-dimensional (0D), systems are materials which have one, two and three, dimensions in the nanometer range, respectively.

The fact that the real space passes from three to one dimension, so as the reciprocal space, has important consequences both on the crystal and the electronic structure. Firstly, we can model the electronic energy

of such a system using the free electron model. This approximation is justified by the fact that valence electrons in metals form a gas that is free to move in the solid. Moreover, being one-dimensional, there is only one direction worth studying. Therefore the wave vector $\vec{k}$ in the reciprocal space is, in fact, a number. The dispersion relation can hence be written as:

$$\varepsilon_k = \frac{\hbar^2 k^2}{2m_e} \tag{1.2}$$

where $\hbar$ is the reduced Planck constant, k is the electron's wave number and m_e is the mass of the electron. In figure 1.2, the dispersion relation obtained from equation 1.2 is plotted over the 1^{st} Brillouin zone (1BZ). $2a$ is the length of the unit cell (cfr. figure 1.3) and ε_F is the Fermi energy. The dispersion relation has the typical shape of a parabola (continuous line in the figure), while the Fermi level (dashed line) sets the Fermi surface, that here is composed of two points, namely $-k_F$ and $+k_F$. Since the dispersion relation is often symmetric with respect to $k = 0$, just one of the two halves is shown, the irreducible Brillouin zone (IBZ).

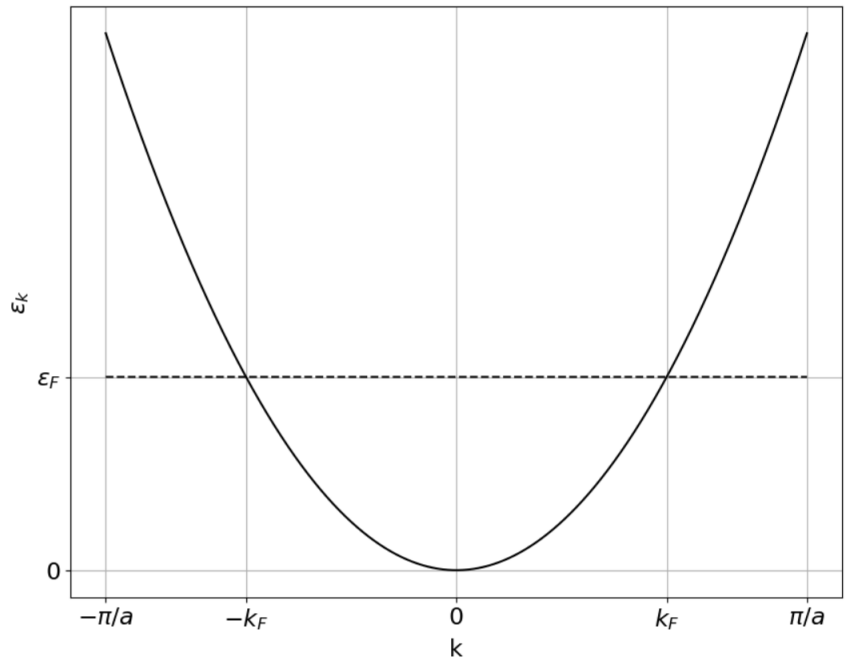

Figure 1.2: Theoretical electronic band structure of a 1D system in the First Brillouin zone. a is half of the size of the unit cell. The continuous line is the dispersion relation, while the dashed one is the Fermi level. We can notice that the Fermi surface is composed of two points.

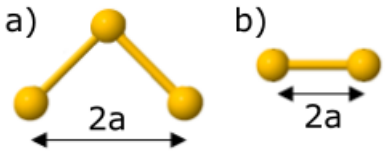

Figure 1.3: Two possible geometries of a nanowire. a) zigzag chain and b) linear chain. Adapted from [17].

1.3 Lindhard response function

At this point, the charge density, ρ, should be introduced. This describes the density of charge as a function of the position in real space, $\rho(\vec{r})$, or in reciprocal space, $\rho(\vec{q})$; the two are related through

$$\rho(\vec{r}) = \int_{\vec{q}} \rho(\vec{q}) e^{i\vec{q}\cdot\vec{r}} d\vec{q} \tag{1.3}$$

The peculiar shape of the Fermi surface leads to a response to external perturbations that is different from the one of 2D and 3D systems [16]. The response of the charge density to a time independent perturbation potential of the form:

$$\phi(\vec{r}) = \int_{\vec{q}} \phi(\vec{q}) e^{i\vec{q}\cdot\vec{r}} d\vec{q} \tag{1.4}$$

is usually treated in the linear response theory:

$$\rho(\vec{q}) = \chi(\vec{q})\phi(\vec{q}) \tag{1.5}$$

where $\chi(\vec{q})$ is the Lindhard response function. It is a complex function that in d-dimensions can be expressed as

$$\mathcal{R}e\{\chi_0(\vec{q})\} = \int \frac{dk}{(2\pi)^d} \frac{f_k - f_{k+q}}{\varepsilon_k - \varepsilon_{k+q}} \tag{1.6}$$

$$\frac{\mathcal{I}m\{\chi_0(q)\}}{\omega} = \int \delta(\varepsilon_k - \varepsilon_F)\delta(\varepsilon_{k+q} - \varepsilon_F) dk \tag{1.7}$$

In equations 1.6 and 1.7, the zero as subscript indicates that the Lindhard function is evaluated close to $\omega = 0$; $f_k = f(\varepsilon_k)$ is the Fermi-Dirac distribution function at wave vector k.

$$f(\varepsilon_k) = \frac{1}{e^{\frac{\varepsilon_k - \varepsilon_F}{k_B T}} + 1}$$

T is the temperature and k_B the Boltzmann constant. It is assumed that the dispersion near the Fermi level is linear, $\varepsilon_k - \varepsilon_F = \hbar v_F(k - k_F)$, where v_F is the Fermi velocity that can be defined as $\hbar k = m_e v_F$. Therefore,

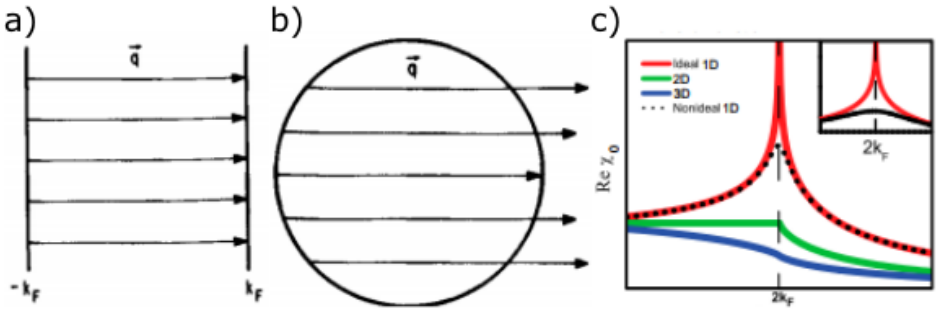

Figure 1.4: Difference in nesting between 1D, 2D and 3D systems: a) nesting vector for a 1D system and b) for a 2D (adapted from [16]). Panel c) illustrates the Lindhard response function for a 1D, 2D and 3D structure; the dashed line shows the effect of a 2 % deviation from perfect nesting (adapted from [18]).

in one dimension, the integral in equation 1.6 has a simple solution that writes:

$$\mathcal{R}e\{\chi_0(q)\} = e^2 n(\varepsilon_F) \log\left|\frac{q-2k_F}{q+2k_F}\right| \tag{1.8}$$

e is the electron's charge and $n(\varepsilon_F)$ is the density of state at the Fermi level defined as

$$n(\varepsilon_F) = \frac{L}{\pi\hbar}\sqrt{\frac{m_e}{2\varepsilon_F}} \tag{1.9}$$

For a phonon's wave vector that fulfills the relation $q = 2k_F$, the response function shows a logarithmic divergence, contrarily to what happens in 2D and 3D (cfr. figure 1.4).

The divergence comes from the fact that there are two states at the same energy, one full and one empty, which differ exactly by $2k_F$: this is called perfect Fermi surface nesting (FSN). Due to the particular topology of the Fermi surface, in 1D there is a large number of states that fulfill this condition and that is why the divergence occurs. For 2D and 3D, the number of states that satisfy it is reduced and the divergence is removed (cfr. figure 1.4). In figure 1.4 a) and b), the difference between perfect nesting with a vector $\vec{q}$ in 1D and 2D is shown. The instability is much more visible in the 1D case since there are many states that differ exactly by the vector $\vec{q}$, while, for instance, in 2D there is only one state. This difference is reflected in the $\chi(\vec{q})$ function, depicted in figure 1.4 c), where the divergence at $q = 2k_F$ is present for the 1D system, ideal or broaden, but not for the 2D and 3D.

1.4 Peierls transition

The diverging behavior for $\chi(\vec{q})$ near $q = 2k_F$ has consequences. Firstly, from equation 1.5, it can be noted that a divergent χ leads to a divergent charge redistribution; from this follows that the electron gas is unstable and the periodicity of the electron gas itself is varied. As stated by Peierls in its work of 1930 [2], a perfect, or quasi-, 1D system is unstable, showing an electronic divergence at the wave vector $2k_F$. As a consequence, the periodicity of the chain is changed and the number of atoms per unit cell doubles. Moreover, the dimension of the 1BZ is divided by two ($\pi/a \rightarrow \pi/2a$) and a gap is opened at its boundary. In figure 1.5, the Peierls transition is shown. On the one hand, in panel a), the situation for a high-temperature conductive system is represented. As mentioned in section 1.1, the charge distribution for a metal at high temperature is highly uniform and the atoms in the chain are evenly spaced. The dispersion relation is the one typical of a conductive system (indeed there are occupied states around the Fermi level). On the other hand, in panel b), the situation where the CDW and the Peierls transition arise is portrayed. Here, the charge density assumes a periodic spacial modulation (cfr. equation 1.1). As a consequence, the unit cell dimension doubles and, therefore, the number of atoms per unit cell doubles as well. Moreover, the dispersion relation becomes the one of an insulator: a gap at the boundary of the new 1BZ is opened.

The opening of the gap leads to a lowering of the electronic energy that is proportional to the amplitude of the lattice's distortion u. For small displacements it goes as $u^2 \log(u)$ [1]. This gain in energy always overcomes the energy needed for the structural relaxation. Therefore, at any temperature lower than T_{CDW}, a 1D system will always undergo the transition [18]. When increasing the temperature from $T = 0\ K$, the electrons start to overcome the energy gap and the CDW condensate progressively loses electrons. This phenomenon becomes more and more relevant up to $T = T_{CDW}$ where a second-order phase transition takes place and the gap is closed. The phase transition can be described following the work by Grüner [1]. Starting from the Ginzburg-Landau theory for such a transition, the electron energy gap at $T = 0\ K$ (Δ_0) can be retrieved

$$\Delta_0 = 2De^{-\frac{1}{\lambda}} \tag{1.10}$$

D is the cut-off energy, i.e. half of the maximum width of the bandgap. λ is defined as

$$\lambda = \frac{g^2(2k_F)}{\omega(2k_F)\epsilon_F}$$

where g is the electron-phonon coupling matrix element (more details

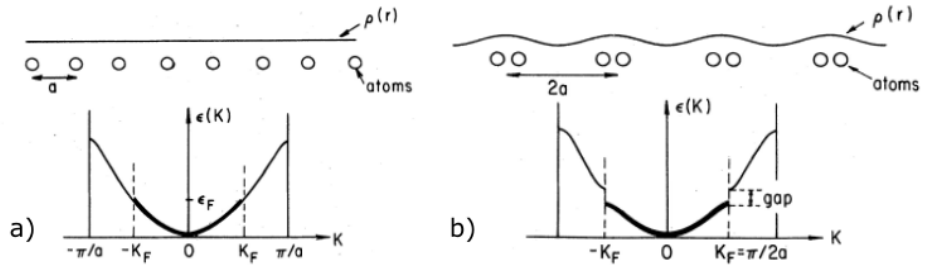

Figure 1.5: Schematic representation of a Peierls transition. In panel a) the system at $T > T_{CDW}$ is represented while in panel b) $T < T_{CDW}$. At the top of the figure the charge density is depicted: it is uniform at a high temperature a), while it assumes the periodic spacial modulation in b). Below, the doubling of the number of atoms in the unit cell is displayed. At the bottom, the metal-insulator transition is depicted; indeed panel a) shows the dispersion relation of a metallic system, while in b) the dispersion relation becomes the one of an insulator. Adapted from [1]

will be provided in section 1.6) and $\omega(2k_F)$ is the phonon frequency at $q = 2k_F$. Similarly, the transition temperature can be written as $T_{CDW} = \Delta_0/1.76k_B$, where the coefficient 1.76 is an experimental value that comes from the BCS theory for superconductivity. It can be already noted that the interplay between phonons and electrons is important. As a matter of fact, the larger the electron-phonon matrix element, the larger λ and, therefore, the band gap are.

A quantitative measurement of the nesting is represented by the low-frequency imaginary part of the electronic susceptibility $\mathcal{I}\mathrm{m}\{\chi_0(\vec{q})\}$ [19]. This must have a peak at the same $\vec{q}$ as the CDW. Moreover, in order to have the transition, the real part of χ needs to have a peak too, since this is the function that drives the instability, as shown in the previous section. As a consequence, all the phonon modes should soften at this wave vector with the sole exception of those forbidden due to symmetry reasons.

There is a common misconception [19] that should be clarified: the distortion of the lattice is not a consequence of the electronic instability. Indeed, if it was so, the electrons could induce a charge redistribution without taking into account whether the lattice would follow or not. The two transitions occur simultaneously one as the cause and consequence of the other. The Fermi surface nesting cannot be considered a sufficient condition for the relaxation of the structure: the phonon dynamics and the electron-phonon interaction have to be taken into account as well.

1.5 Kohn anomaly

Kohn [14] was the first to point out that the lattice vibrations are screened out by the conductive electrons in metals. At some point $\vec{q}$ in the reciprocal space, this screening changes abruptly; therefore, the phonon frequency ω varies accordingly at the very same $\vec{q}$, in the following manner

$$\left|\nabla_{\vec{q}}\,\omega(\vec{q})\right| \to \infty \tag{1.11}$$

where $\nabla_{\vec{q}}$ is the gradient with respect to $\vec{q}$. The position of these points is determined, as mentioned above, by the Fermi surface nesting. In Kohn's picture, the physical origin of this abrupt change comes from the embedded charge distribution $\rho_{ext}(\vec{r})$ that induces an electronic charge density

$$\rho_{el}(\vec{r}) = -F(\vec{q})\rho_{ext}(\vec{r})$$

where

$$F(\vec{q}) = \frac{\mathcal{R}e\{\chi_0(\vec{q})\}}{\vec{q}}$$

The function $\chi(\vec{q})$ can be expressed as in equation 1.8. Now, if the derivative of F is evaluated close to $q = 2k_F$ it can be noted that

$$\frac{d\mathcal{R}e\{\chi(q)\}}{dq}\Big|_{q\sim 2k_F} \propto \log|q - 2k_F|\Big|_{q\sim 2k_F} \to -\infty$$

Equation 1.11 is a consequence of this. This abrupt change is due to the fact that for the phonon wavevector $q > 2k_F$ electrons cannot screen anymore the charge distribution and, contrarily to what happens when $q < 2k_F$, the charge distribution cannot cause virtual excitations that conserve the energy (cfr. figure 1.6a) and b))

The consequence of equation 1.11 on the phonon band structure is that near $q = 2k_F$ all the phonon modes (at least those which are not forbidden by symmetry reasons) will soften and there will be a dip with slope theoretically infinite. However, the magnitude of the softening is driven by temperature. Therefore at high enough temperatures the softening will be washed out, while it will become more and more important as the temperature decreases. When the phonon frequency will reach $\omega^2 = 0$, the mode will become unstable and the structure will relax. However, if the softening does not take place at the boundary of the 1BZ, the metal-insulator transition, typical of the Peierls picture, is not guaranteed to occur. In Ref. [6], an example of a quasi-1D system ($NbSe_3$) is reported. This system shows two anomalies at temperatures 149 and $59\ K$, but neither of them results in a metal-insulator transition (cfr. figure 5b in the reference). The temperature that corresponds to

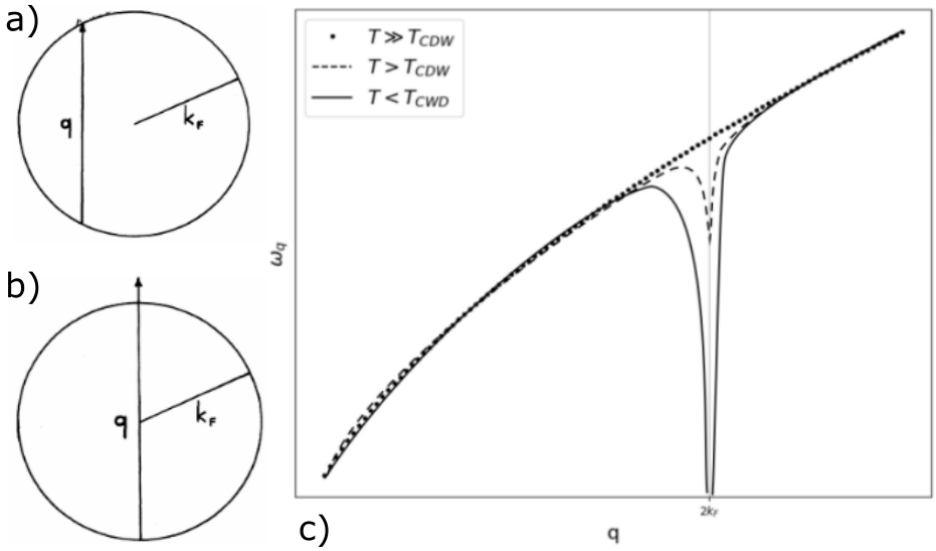

Figure 1.6: Virtual excitation for a) $q < 2k_F$ and b) $q > 2k_F$. Adapted from [14]. c) Schematic representation of Kohn anomaly: the dotted line is the high temperature phonon dispersion relation; the dashed line is the Kohn anomaly, which however does not lead to a structural relaxation since the temperature is still higher than the transition temperature; the continuous line is the dispersion at a temperature lower than the transition temperature: the mode becomes unstable and the Peierls transition takes place. Inspired by Ref. [18].

this transition is again referred to as T_{CDW}. If there is a softening of the phonon mode, but the frequency does not become negative, there will be no structural relaxation. In figure 1.6c) the phonon dispersion relation around the point $q = 2k_F$ is shown. The dotted line portrays the band at $T \gg T_{CDW}$ where the Kohn anomaly is totally cancelled. The dashed line corresponds to a temperature that is still above T_{CDW} but in the same order of magnitude. In this case, a softening can be seen, even though no lattice distortion will take place. Finally, the continuous line displays the situation at a temperature below the transition temperature: the phonon frequency becomes negative which means that now the system is unstable and the structural relaxation occurs.

It is immediately clear that, as for Peierls transitions, Kohn anomalies are not the result of some phonon dynamics on their own, but they involve the need of an interplay between the conductive electrons and phonons; it will therefore be needed to explore the electron-phonon interactions.

1.6 Electron-phonon coupling

The need to introduce electron-phonon coupling (EPC) derives from the fact that the vision for which Peierls instabilities and Kohn anomalies are due to electrons or phonons instabilities alone is incomplete. As pointed out by Johannes and Mazin [19], the problem with Kohn and Peierls theories is that every time there is a FSN all the phonon modes, except for the ones that are forbidden for symmetry reasons, should soften. However, this is almost never the case. It is not rare to observe, at a certain $q = 2k_F$ that just one mode softens, or none. This is because the main actor in the formation of Kohn anomalies is the EPC. In order to see a large dip in the phonon band structure, a large electron-phonon interaction has to be present.

In this section, the problem will be set and the main results will be introduced, without deriving them (for derivations one can consult the work of Giustino [20]).

In order to analytically analyze the electron-phonon coupling, one should start from the Hamiltonian describing a coupled electron-phonon system [20]:

$$\hat{H} = \hat{H}_e + \hat{H}_{ph} + \hat{H}_{e-ph} \tag{1.12}$$

where

$$\hat{H}_e = \sum_{n\vec{k}} \varepsilon_{n\vec{k}} \hat{c}^+_{n\vec{k}} \hat{c}_{n\vec{k}}$$

is the Hamiltonian part that describes non-interacting electrons and $\varepsilon_{n\vec{k}}$ is the eigenvalue of an electron in band n with crystal momentum $\vec{k}$

$$\hat{H}_{ph} = \sum_{\vec{q}\nu} \hbar\omega_{\vec{q}\nu} \left(\hat{a}^+_{\vec{q}\nu} \hat{a}_{\vec{q}\nu} + \frac{1}{2} \right)$$

is the non-interacting-phonon Hamiltonian, where $\omega_{\vec{q}\nu}$ is the frequency of lattice vibration with crystal momentum $\vec{q}$ and mode ν. Finally,

$$\hat{H}_{e-ph} = \frac{1}{\sqrt{N_p}} \sum_{n\vec{k},\nu\vec{q}} g_{n,m,\nu}\left(\vec{k},\vec{q}\right) \hat{c}^+_{n\vec{k}+\vec{q}} \hat{c}_{n\vec{k}} (\hat{a}_{\vec{q}\nu} + \hat{a}^+_{-\vec{q}\nu})$$

describes the electron-phonon coupling at the first order in atomic displacements. N_p is the number of unit cells in the Born-von-Karman supercell, $g_{n,m,\nu}\left(\vec{k},\vec{q}\right)$ is the electron-phonon matrix element and it has the dimensions of an energy. Furthermore, it measures the strength of the coupling between the electron in band n with wave vector $\vec{k}$ and the phonon in branch ν with wave vector $\vec{q}$ to the electron state in band m

with wave vector $\vec{k}+\vec{q}$. Then, $\hat{c}^{+}_{n\vec{k}}$,$\hat{c}_{n\vec{k}}$ and $\hat{a}^{+}_{\vec{q}\nu}$,$\hat{a}_{\vec{q}\nu}$ are the fermionic and bosonic creation and destruction operators, respectively.
The electron-phonon coupling matrix element can be evaluated through

$$g_{n,m,\nu}\left(\vec{k},\vec{q}\right) = \langle \psi_{m\vec{k}+\vec{q}} | \Delta_{\nu\vec{q}} V | \psi_{n\vec{k}} \rangle \tag{1.13}$$

where ψ is the electronic wave function at band n (m) with wave vector $\vec{k}$ ($\vec{k}+\vec{q}$). $\Delta_{\nu\vec{q}}V$ is the first order variation of the potential for a perturbation at mode ν and phonon wavevector $\vec{q}$.

Therefore, it will be important to evaluate all these quantities to characterize the various instabilities, i.e. electron energies, phonon frequencies and EPC matrix elements. It will also be interesting to see how the first order variation of the potential evolves around the FSN.

For the time being, following the work by Barnett *et al.* [21], an analytical expression for the phonon frequencies close to $q = 2k_F$ can be found. The phonon self-energy of the mode ν at the wave vector $\vec{q}$ can be written as:

$$\Pi_{\mu}(\vec{q}) = 2\sum_{n} |g_{n,m,\nu}(\vec{k},\vec{q})|^2 \chi_{0,n}(\vec{q}) \tag{1.14}$$

In equation 1.14, χ is the electronic susceptibility defined in equation 1.6. The dressed frequencies, for mode ν and phonon wave vector $\vec{q}$, will be:

$$(\omega_{\nu,\vec{q}})^2 = (\omega^0_{\nu,\vec{q}})^2 + 2\omega^0_{\nu,\vec{q}}\Pi_{\nu}(q) \tag{1.15}$$

Here $\omega^0_{\mu,\vec{q}}$ is the undressed frequency. Substituting equation 1.14 and 1.8 in equation 1.15, we can write the dressed frequencies as:

$$\begin{aligned}(\omega_{\nu,\vec{q}})^2 &= (\omega^0_{\nu,\vec{q}})^2 \\ &+ \sum_{n} (2\omega^0_q MNN_c)|g_{\nu,n,m}(\vec{k},\vec{q})|^2 \frac{2m^*a}{\pi MN_c k_{F,n}} \log\left|\frac{2k_{F,n}-q}{2k_{F,n}+q}\right|\end{aligned} \tag{1.16}$$

This shows that near the nesting vectors there are logarithmic divergences that are proportional to the squared modulus of the electron-phonon matrix elements, and that depend on the phonon modes ν and on the different electronic bands n. From this equation, it is clear that, firstly, Fermi surface nesting alone is not enough to see a dip in the phonon dispersion relation. As a matter of fact if $|g_{\nu,n,m}(\vec{k},\vec{q})|^2$ is zero (no EPC), then the sum in equation 1.16 is zero and the phonon frequency is the undressed one; no dip is thus observed. Moreover, not all the modes will soften but, since the EPC matrix element is depending on the mode ν, only the modes with a large $|g|^2$ will damp.

Lastly, a further correction can be introduced. If the Coulomb repulsion $V(q)$ is introduced in equation 1.15, this can be rewritten as [21]:

$$(\omega_{\nu,\vec{q}})^2 = (\omega^0_{\nu,\vec{q}})^2 + 2\omega^0_{\nu,\vec{q}}\frac{\Pi_\nu(q)}{1 - V(q)\chi_0(q)} \tag{1.17}$$

It can be noted that a large Coulomb interaction can suppress the CDW instability. The physical origin of this term is that the electronic Coulomb repulsion can screen the electron-phonon coupling and therefore cancel the CDW.

1.7 Final remarks

In the sections above, the Fermi surface nesting has always been referred to as $q = 2k_F$. However, this comes from the fact that a parabolic dispersion relation was assumed and from the fact that just one electronic band would cross the Fermi level.

In the case in which two bands cross the Fermi level as in the case depicted in figure 1.7, or even in the case in which one band crosses the Fermi level multiple times, there will be multiple $\vec{q}$ that will connect two points on the Fermi level (an example will be provided in chapter 2). In these cases, nesting refers, not only to the phenomenon that takes place at $q = 2k_F$, but to all the $\vec{q}$ vectors in reciprocal space that allow electrons to make transitions of the type $k^1_F \rightarrow k^2_F$. Continuing with the example in figure 1.7, there will be four Fermi surface nestings, that are depicted in the figure with four arrows:

- $q_A : -k^1_F \rightarrow k^1_F$
- $q_B : -k^2_F \rightarrow k^2_F$
- $q_C : -k^2_F \rightarrow k^1_F$
- $q_D : \ k^2_F \rightarrow k^1_F$

As a result of these four FSN, equation 1.6 will exhibit four terms that lead to a divergence [24].

$$\chi(\vec{q}) = \frac{1}{2\pi}\Big(\int \frac{f^1_k - f^1_{k+q}}{\epsilon^1_k - \epsilon^1_{k+q}}dk + \int \frac{f^2_k - f^2_{k+q}}{\epsilon^2_k - \epsilon^2_{k+q}}dk + \int \frac{f^2_k - f^1_{k+q}}{\epsilon^2_k - \epsilon^1_{k+q}}dk + \int \frac{f^1_k - f^2_{k+q}}{\epsilon^1_k - \epsilon^2_{k+q}}dk\Big) \tag{1.18}$$

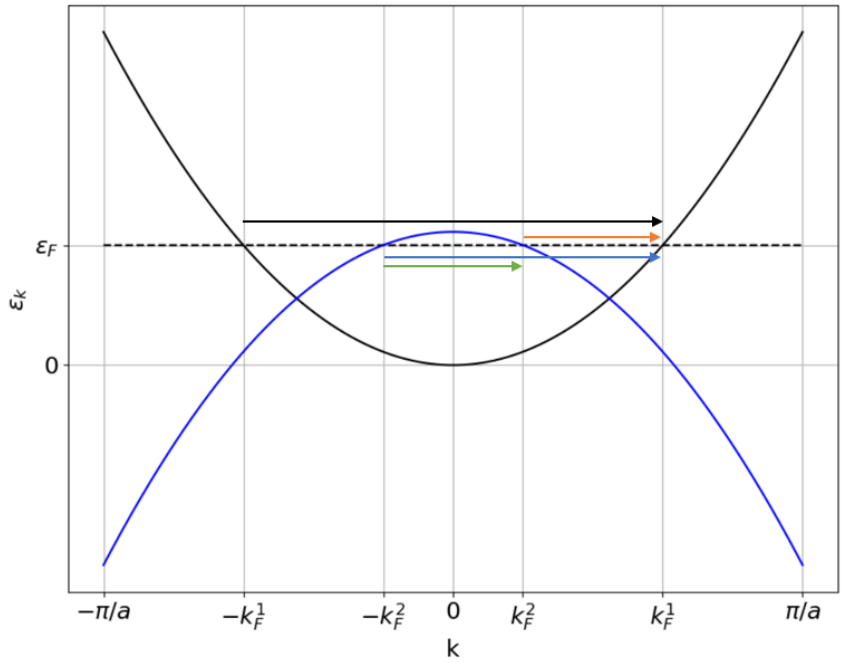

Figure 1.7: Nesting for a Fermi surface composed by more than two points.

Therefore, the equation to retrieve the dressed phonon frequency shown in section 1.6 has to be adapted as well [21]

$$(\omega_{\nu,\vec{q}})^2 = (\omega^0_{\nu,\vec{q}})^2 + D_A \log\left|\frac{2k_F^1 - q}{2k_F^1 - q}\right| + D_B \log\left|\frac{2k_F^2 - q}{2k_F^2 - q}\right| + D_C \log\left|\frac{(k_F^1 + k_F^2) - q}{(k_F^1 + k_F^2) - q}\right| + D_D \log\left|\frac{(k_F^1 - k_F^2) - q}{(k_F^1 - k_F^2) - q}\right| \quad (1.19)$$

where, D_i, $i \in \{A, B, C, D\}$, is the factor multiplying the logarithm in equation 1.16, but for the different k_F.

To sum up, as stated in this chapter, the elements that are needed for a system to show a charge density wave instability are (i) a nesting of the Fermi surface, (ii) which should lead to a divergence in the real part of the Lindhard function and (iii) a large EPC matrix element should be present for at least one mode.

Concluding the chapter, it is worth mentioning that throughout this work the various properties will be simulated from first principles. However, they can be measured in the following manner: X-ray scattering can probe the temperature dependence of the Kohn anomaly in the phonon dispersion [15]; transport measurement can reveal the transition temperature between the conductive and insulating phase, i.e. the Peierls tran-

sition [25]; finally, high-resolution angle-resolved photoemission spectroscopy [26] (ARPES) can detect the strength of EPC in a CWD system.

Chapter 2

Results and discussion

In this chapter the obtained results will be presented. The physical results of the computations will be explained and comparisons between the different systems will be made. Moreover, several considerations on the computational methods and the techniques used to improve the calculations' feasibility will be given. An extensive study on the linear chain is carried out in order to understand the physics and the principle of CDWs. The goal is to apply the acquired notions to the case of 3D systems. The chapter is organized as follows: in section 2.1, the chosen structure and the parameters involved are introduced; in section 2.2, the used DFT and DFPT techniques for the various steps are briefly explained; eventually, in sections 2.3 and 2.5, the results obtained for the silicon and aluminum chains, are discussed. At the end of the chapter, some results on the bulk structure of silicon and aluminum are presented.

2.1 Structure

2.1.1 Description of system and parameters

The systems studied are linear chains of aluminum (atomic number $Z = 13$) and silicon ($Z = 14$). The structure is composed of one atom per unit cell which is tetragonal (cfr. figure 1.3b)). The length of the cell along the wire axis matches the Si-Si (Al-Al) bond length. The two perpendicular dimensions are chosen to be equal and large enough to provide enough vacuum between the chains. Indeed, ABINIT uses periodic boundary conditions in all the spacial directions; therefore, enough vacuum has to be ensured in order to avoid interactions between the adjacent nanowires. The chosen vacuum is 10 Å because it has been proven to ensure decoupling between nanowires (cfr. appendix A).

As we shall see, both materials are metallic. As a result, it is needed to face the problem of approximating the Fermi-Dirac (FD) distribution function around the Fermi level at finite temperature. The solution usually employed is to simulate the behavior of the FD distribution with a smearing function. This needs to be enough accurate, but, at the same time, to ensure a fast convergence and feasibility in terms of numerical computation. Here, the smearing used is Gaussian, which corresponds to the 0-order Hermite polynomial of Methfessel and Paxton [30]. The smeared δ function can be written as

$$\tilde{\delta}(x) = \frac{e^{-x^2}}{\sqrt{\pi}}$$

and the occupancy is its integral:

$$f(x) = \frac{1}{2}[1 - \mathrm{erf}(x)] \tag{2.1}$$

As a consequence of this approximation, the parameter that governs temperature is the smearing temperature (or electronic temperature), which has the dimensions of an energy. Actually, temperature and energy of a system are strictly connected by the relation $E \propto k_B T$, where k_B is the Boltzmann constant. Even though this is not a physical quantity, lowering the value of this parameter one can simulate the effect of decreasing the temperature. In the following, the smearing temperature will be referred to as temperature, always keeping in mind that actually it is not.

2.1.2 Structural relaxation

The structures have been relaxed. This means that the cell is allowed to change its dimension in order to reach the minimum in energy. Dealing with systems like the one described above, the only degree of freedom is the bond length along the NW axis. The dimensions of the relaxed structure depend on the parameters used to simulate the system (they are described in appendix A). Therefore, these need to be carefully converged. The relaxed bond lengths are 2.204 Å for silicon and 2.42 Å for aluminum.

The results will be presented in the following manner: for each structure, the electronic dispersion relation will be discussed. As stated in chapter 1, the shape of the electronic band structure is important to determine the shape of the Fermi surface and hence the possible FSN. Afterwards, the phononic dispersion relation will be shown and the strength

of the eventual Kohn anomalies examined. At the end, the EPC matrix elements and the first order perturbation of the potential will be computed.

2.2 Methodology

In this section, the main references about the methods used in order to retrieve the different physical quantities are introduced.

2.2.1 Electron band structure

Firstly, the electronic band structure is extracted solving the Kohn-Sham (KS) equation non-self-consistently at different points in the 1BZ (cfr. equation 2.2 and Ref. [31, 32]). The used electronic density comes from a previous ground state self-consistent computation.

$$\hat{H}^{KS}\psi_n^{KS}(\vec{r}) = \varepsilon_n^{KS}\psi_n^{KS}(\vec{r}) \tag{2.2}$$

The Kohn-Sham Hamiltionian has the following form

$$\hat{H}^{KS} = -\frac{1}{2}\nabla^2 + V^{KS}(\vec{r}) \tag{2.3}$$

In equation 2.3, the first term on the right-hand side is the kinetic energy, while the second is the KS potential. It is the potential for a single electron which is expressed as

$$V^{KS}(\vec{r}) = V^{ext}(\vec{r}) + V^{H}(\vec{r}) + V^{xc}(\vec{r}) \tag{2.4}$$

where $V^{ext}(\vec{r})$ is the potential seen by the single electron due to the presence of the nucleus. $V^{H}(\vec{r})$ is the Hartree potential

$$V^{H} = \int d\vec{r'} \frac{n_e(\vec{r})}{|\vec{r} - \vec{r'}|}$$

where $n_e = \sum_n |\psi_n|^2$ is the electron density. As it can be noted from the equation, the Hartree potential takes into account the effect of the other electrons in the atom. Lastly, $V^{xc}(\vec{r})$ is the exchange-correlation potential

$$V^{xc}(\vec{r}) = \frac{\delta E^{xc}[n_e]}{\delta n_e}$$

which has to be modeled with a choice of the pseudopotential. Among all the choices, the most popular are usually the LDA and GGA.

In this work, V^{xc} is modeled with the PBEsol functional [27]. The used pseudopotentials are optimized norm-conserving ONCVPSP [28, 29]. The electronic configurations of the two species are $[Ne]3s^23p^1$ for aluminum and $[Ne]3s^23p^2$ for silicon (the configuration of neon is $1s^22s^22p^6$). The chosen pseudopotential considers ten core electrons for both species and three (four) valence electrons for Al (Si).

2.2.2 Phonon band structure

The phonon dispersion relation is calculated using the Density Functional Perturbation Theory (DFPT) [33–38]. The idea is to calculate the second order derivative of the total energy which is connected to the phonon dynamical matrices. In order to do that, a perturbation corresponding to the displacement of each atom in the unit cell needs to be applied in the three spatial directions. From these matrices, the phonon frequency can be directly calculated. However, this is done explicitly only for some points in the reciprocal space; how many and how they are positioned will be subject to discussion. Afterwards, these will be interpolated using different schemes, i.e. Fourier transform (FT) and spline.

The DFPT formalism has origin in the perturbation theory. The details of this theory may be found in several textbooks, for instance Ref. [40]. The idea is to start from a Schrödinger equation

$$H^{(0)}\psi^{(0)} = \varepsilon^{(0)}\psi^{(0)}$$

whose solutions are known (denoted with a superscript (0)), and to apply a small perturbation in the following manner

$$\hat{H} = \hat{H}^{(0)} + \lambda\hat{H}^{(1)} + \lambda^2\hat{H}^{(2)} + ... \tag{2.5}$$

where $H^{(i)}$ are the perturbative terms and λ is a small number. In the same way, the wave function and every physical quantity X can be expressed as

$$X = X^{(0)} + \lambda X^{(1)} + \lambda^2 X^{(2)} + ... \tag{2.6}$$

Solving the Schrödinger equation $\hat{H}\psi = \varepsilon\psi$ using the Hamiltonian in 2.5 and the wave function of the form in equation 2.6, the first and second order correction of the energy are respectively:

$$\varepsilon^{(1)} = \langle\psi_n^{(0)}|H^{(1)}|\psi_n^{(0)}\rangle \tag{2.7}$$

$$\varepsilon^{(2)} = \sum_{n\neq m} \frac{|\langle\psi_m^{(0)}|H^{(1)}|\psi_n^{(0)}\rangle|^2}{\varepsilon_n^0 - \varepsilon_m^{(0)}} \tag{2.8}$$

where n and m are the electronic bands.

The second order correction of the energy can also be expressed as a function of the perturbation associated with the atomic displacement mentioned above:

$$\varepsilon = \varepsilon^{(0)} + \frac{1}{2} \sum_{(\kappa,\alpha,p)} \sum_{(\kappa',\alpha',p')} \frac{\partial^2 \varepsilon}{\partial \tau^p_{\kappa,\alpha} \partial \tau^{p'}_{\kappa',\alpha'}} u^p_{\kappa,\alpha} u^{p'}_{\kappa',\alpha'} \tag{2.9}$$

where $\tau^p_{\kappa,\alpha}$ is the position of the atom κ in the unit cell p, along the cartesian coordinate α. $u^p_{\kappa,\alpha}$ is the corresponding displacement of the atom with respect to its equilibrium position. The interatomic force constants (IFCs) are

$$C^{pp'}_{\kappa\alpha,\kappa'\alpha'} = \frac{\partial^2 \varepsilon}{\partial \tau^p_{\kappa,\alpha} \partial \tau^{p'}_{\kappa',\alpha'}} \tag{2.10}$$

The dynamical matrices are defined as

$$\tilde{D}_{\kappa\alpha,\kappa'\alpha'}(\vec{q}) = \frac{1}{M_\kappa M_{\kappa'}} \tilde{C}_{\kappa\alpha,\kappa'\alpha'}(\vec{q}) \tag{2.11}$$

where M_κ is the mass of the atom κ and the tilde indicates the Fourier transform. Then, the squared phonon frequencies $\omega^2_{\vec{q}\nu}$ can be obtained solving the following eigenvalue problem

$$\sum_{\kappa'\alpha'} \tilde{C}_{\kappa\alpha,\kappa'\alpha'}(\vec{q}) U_{\kappa'\alpha'\nu}(\vec{q}) = M_\kappa \omega^2_{\vec{q}\nu} U_{\kappa\alpha\nu}(\vec{q}) \tag{2.12}$$

where $U_{\kappa\alpha\nu}(\vec{q})$ is the phonon eigendisplacement, i.e. the vector describing the amplitude of the oscillation of atom κ for a phonon mode ν and wave vector $\vec{q}$.

2.2.3 Electron-phonon coupling matrix elements

The EPC matrix elements are computed starting from DFPT [20, 39]:

$$g_{\nu,n,m}(\vec{k},\vec{q}) = \langle \psi^{KS}_{m\vec{k}+\vec{q}} | \Delta_{\vec{q}\nu} V^{KS} | \psi^{KS}_{n\vec{k}} \rangle \tag{2.13}$$

where $\psi^{KS}_{n\vec{k}}$ is the Kohn-Sham Bloch's state and $\Delta_{\vec{q}\nu} V^{KS}$ is the first-order variation of the self-consistent KS potential. This can be evaluated as

$$\Delta_{\vec{q}\nu} V^{KS} = \frac{1}{\sqrt{2\omega_{\vec{q}\nu}}} \sum_{p,\kappa,\alpha} \frac{\partial V^{KS}}{\partial \tau_{\kappa\alpha}} \frac{e_{\kappa\alpha,\nu}(\vec{q})}{\sqrt{M_\kappa}} e^{i\vec{q}\cdot\vec{R}_p} \tag{2.14}$$

where $e_{\kappa\alpha,\nu}(\vec{q})$ is the α-th Cartesian component of the phonon eigenvector for the atom κ in the unit cell p, M_κ is the atomic mass, τ_κ is its position and $\vec{R}_p$ is the lattice vector that defines the unit cell p. The first-order derivative of the KS potential can be obtained directly from DFPT by solving self-consistently a system of Sternheimer equations [33, 35].

2.3 Silicon nanowire

In this section, the results obtained for silicon NW will be presented together with some details on the computational work. These same concepts will be then exploited in the next section in order to discuss the results found for aluminum NW.

2.3.1 Electron band structure

From the relaxed structures, the electronic dispersion relation of silicon is calculated (cfr. figure 2.1). The calculations have been performed after checking once again the convergence of the electron energy with respect to the cut-off energy and the number of k points in reciprocal space. As already stated, being 1D systems, the only meaningful direction to be studied is the one along the chain axis ($\Gamma - Z$). Looking at the IBZ, it can be noted that there are two points composing the Fermi surface, namely $k_F^A = 0.0\ 0.0\ 0.218$ (that is doubly degenerate) and $k_F^B = 0.0\ 0.0\ 0.435$ (that is non-degenerate). From now on, the points in the reciprocal space will be referred to mentioning only the last number of the coordinate in reciprocal space since this suffices to identify the point.

Firstly, the system is metallic since it is characterized by half-filled bands. Moreover, following the description in section 1.7, there will be four possible FSN wave vectors:

$$\begin{cases} q_A = 2 \times k_F^A = 0.436 \\ q_B = 2 \times k_F^B = 0.872 \\ q_C = |k_F^A - k_F^B| = 0.217 \\ q_D = k_F^A + k_F^B = 0.653 \end{cases} \tag{2.15}$$

Folding them back into the IBZ, they become

$$\begin{cases} q_A = 0.436 \\ q_B = 0.128 \\ q_C = 0.217 \\ q_D = 0.347 \end{cases} \tag{2.16}$$

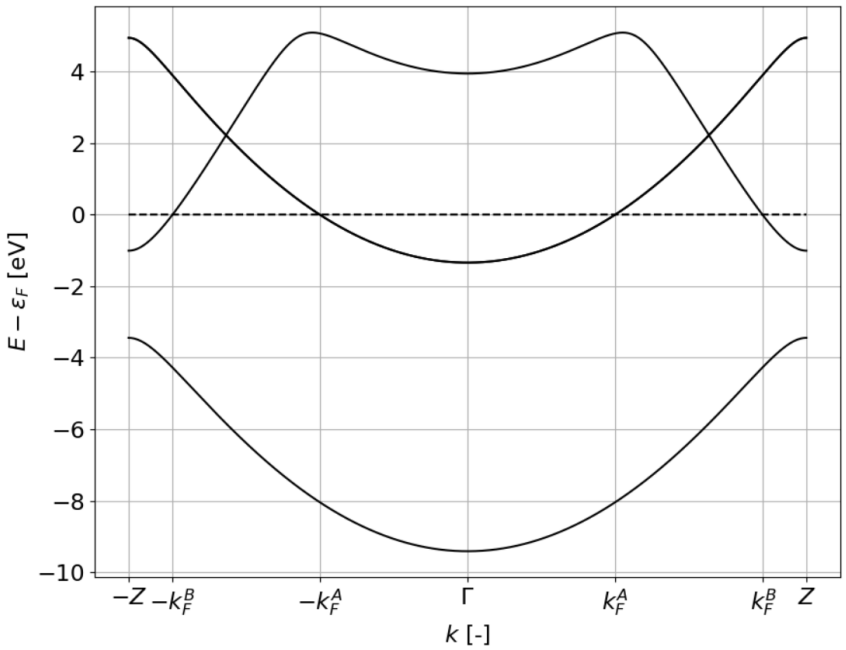

Figure 2.1: Electronic band structures for silicon nanowire. The Fermi level is set to zero and it is represented with a dashed line. The Fermi surface is indicated with the points k_F.

2.3.2 Phonon band structure

In this section, the phonon dispersion relation of silicon NW will be investigated. On the one hand, from the physical point of view, the softening of the phonon modes and the effect of temperature on the instability will be explored. On the other hand, from the computational point of view, the dependence of the band structure on the choice of the q-points and the interpolation scheme will be examined.

Physical description

In figure 2.3, the phonon dispersion relations at three different values of the smearing temperatures are shown. Firstly, it can be noted that there are two phonon modes. Indeed, since there is only one atom per unit cell, the two possible phonon modes are the vibration along the axis (longitudinal) and the one off-axis (transverse), which is actually degenerated. The two possible vibrational modes are depicted in figure 2.2. All the frequencies of the transverse mode are negative; therefore, the mode is unstable. Since the transverse mode is unstable, the zigzag structure should be the most stable (cfr. figure 1.3a)). Indeed, in Ref. [17], He *et al.* show how the unstrained monoatomic gold chain is not stable, while the zigzag is. Here the situation might be similar.

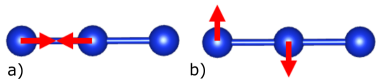

Figure 2.2: Vibrational modes for the monoatomic linear chain: in panel a) longitudinal mode and in panel b) transverse mode.

It can be noted how in correspondence of the nesting vectors, Kohn anomalies can be observed. On the one hand, the longitudinal mode shows two Kohn anomalies: one at q_B and one at q_A. At the former point, it shows a dip that is relatively small at a temperature (tsmear in the graph) of 1×10^{-2} Ha, while it becomes more relevant at lower temperatures. At a temperature of 1×10^{-3} Ha, the mode becomes negative and, hence, it leads to a structural relaxation. At the latter one, the mode softens but the effect is smaller. This Kohn anomaly never leads to an instability; however, it can be noted that at 1×10^{-2} Ha the dip is small and quite broad, while it deepens and shrinks decreasing the temperature. On the other hand, the transverse mode softens at q_C and q_D. Even though the mode is unstable, it shows Kohn anomalies and, hence, it is worth studying. The anomaly at q_C is totally canceled when the temperature is 1×10^{-2} Ha, while it appears at 1×10^{-3} Ha and it is enhanced at 1×10^{-4} Ha. Meanwhile at q_D an anomaly occurs at 1×10^{-4} Ha.

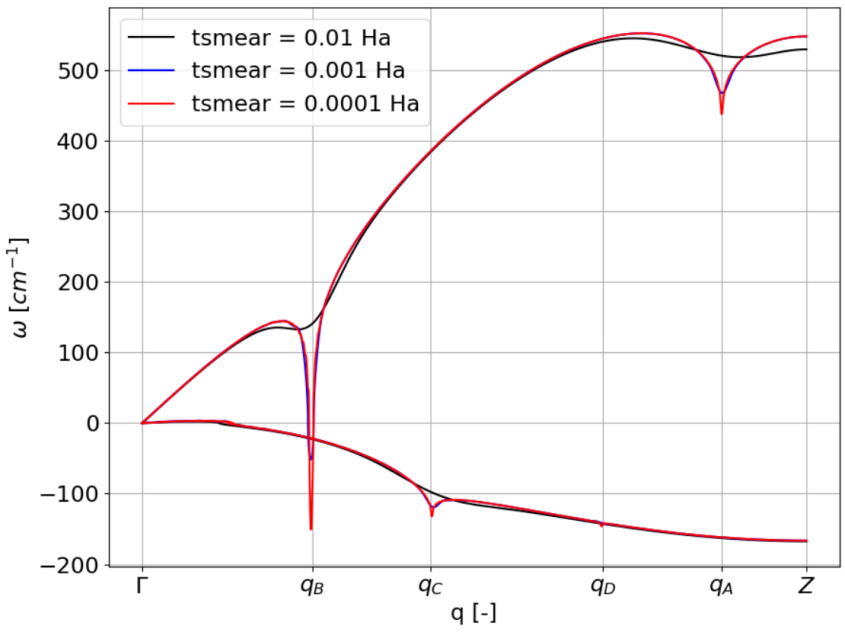

Figure 2.3: Temperature dependent phonon band structure for silicon NW

Summarizing, at the four nesting vectors, one mode for each point

softens and one of them, namely the longitudinal mode at q_B, leads to an instability.

The section can be concluded showing the evolution of the phonon frequency at q_B as a function of the temperature. In figure 2.4, the temperature is plotted on a logarithmic scale. It can be noted that T_{CDW} is in the interval $(5 \times 10^{-3}, 1 \times 10^{-3})$ Ha.

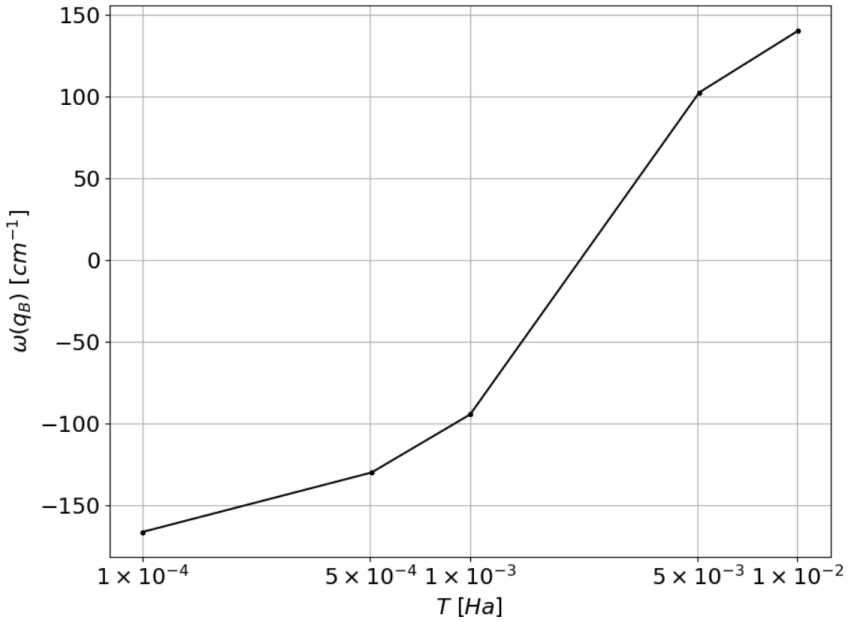

Figure 2.4: Frequency at q_B as a function of the temperature. The temperatures are represented in logarithmic scale.

Computational description

While computing the phonon band structure, a double convergence has to be pursued. On the one hand, the grid of k-points needs to be dense enough in order to get the proper value of the calculated frequencies. On the other hand, the number of q-points at which the phonon frequency is directly calculated has to be high enough. Particularly, in systems where these kinds of anomalies are present, a high number of q-points are needed. Since there is not an algorithm to predict Kohn anomaly, the qs at which the phonon frequency softens have to be calculated directly. Conversely, if the grid is too narrow, the interpolation will not appropriately describe the dips. Figure 2.5 can be studied as an example.

In the graph, the dispersion relation at 1×10^{-3} Ha is plotted. The black curve samples the reciprocal space with 21 on the $\Gamma - Z$ line, while the red one with 101. Therefore, the two grids are commensurate: the black curve passes in one out of five points belonging to the red one. It

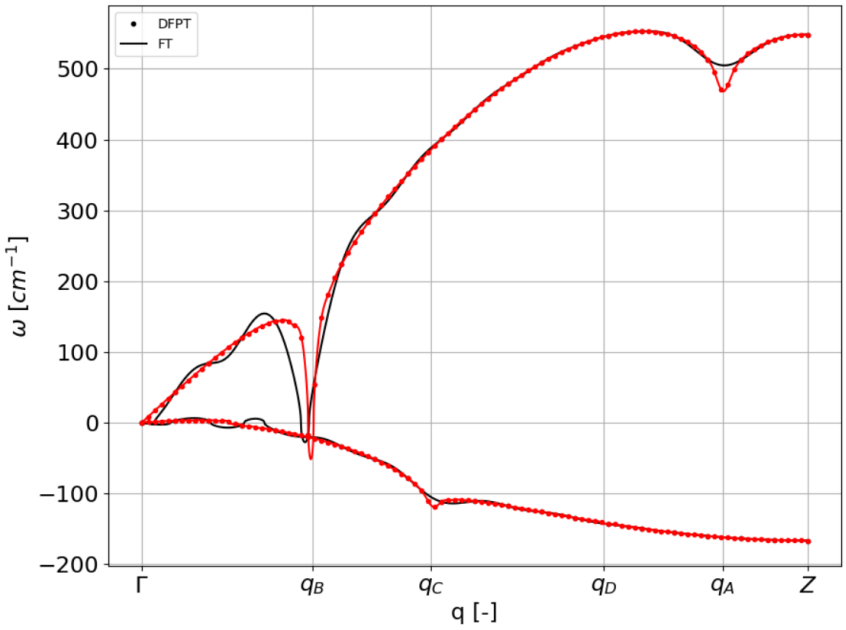

Figure 2.5: Phonon dispersion relation for silicon. The temperature is 1×10^{-3} Ha. The dots are the directly-calculated frequencies, while the continuous line is the Fourier Transform interpolation. The black and red curves are sampled by 21 and a 101 equally-spaced points, respectively.

can be immediately noted that far from the Kohn anomalies and from Γ, the convergence is quite fast and the dispersion relation is well described already with 21 points in the IBZ. However, at the Kohn anomalies it can be observed that the black curve totally misrepresents the real behavior: at q_A and q_C the anomaly is reduced, while at q_B it is displaced at a lower wave vector. Furthermore, between Γ and q_B, the black curve displays some oscillations that are completely nonphysical but just the effect of interpolation. This calls from a careful convergence with respect to the two grids in reciprocal space. Moreover, while lowering the temperature, one has to carefully check on these two convergences and the trend is that finer grids are needed for decreasing temperatures. As a matter of fact, the convergence on the reciprocal-space sampling is summarized in table 2.1.

	1×10^{-2} Ha	1×10^{-3} Ha	1×10^{-4} Ha
k-grid	100	500	3000
q-grid	21	101	501

Table 2.1: Number of reciprocal-space points needed for convergence for of two grids at different temperatures.

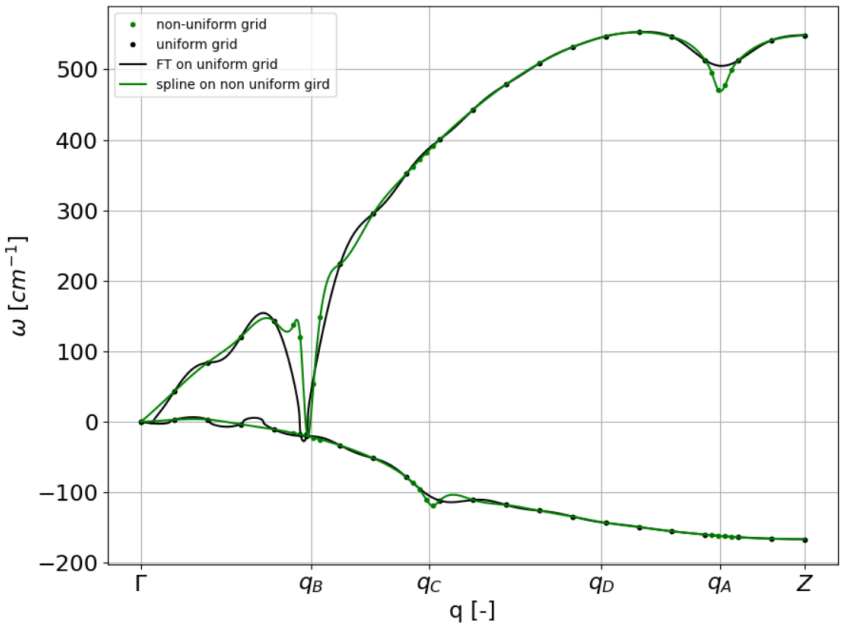

Figure 2.6: Phonon dispersion relation for silicon. The temperature is 1×10^{-3} Ha. The black dots and line are the same as figure 2.5. The green dots form a non-uniform grid: the 21-point grid is used. Around the Kohn anomalies the points belonging to the other grid are added. The green line is an interpolation of these points with a spline.

In Ref. [41, 42], Petretto *et al.* aim at finding a systematical way in order to get the convergence on the two grids for different semiconductors. A similar work should be performed for metals as well. As already stated, the problem with this kind of materials is that the Kohn anomalies should be predicted *a priori*.

A solution to get a more accurate phonon band structure while keeping the number of directly-DFPT-calculated frequencies limited is to use a non-uniform grid (cfr. figure 2.6). Far from the anomalies, the 21-point mesh is used, while close to the anomalies, the 101-point grid is exploited. The result is the green line in the figure. If this is compared with the red line in figure 2.5, it can be noted that the description of the Kohn anomaly is relatively improved with respect to the black line. The advantage of this last method is that only 33 points, instead of the 101, are required to obtain it. The gain here is small since the number of q points for convergence is relatively small, but when it increases, the gain increases too. Furthermore, the spline interpolation scheme has the advantage of not showing the nonphysical oscillations close to Γ, while it has the drawback that it enhances the oscillations around the instabilities.

2.3.3 Electron-phonon coupling matrix elements

As stated in chapter 1, in order to have a complete view over charge density waves, the electron-phonon coupling needs to be taken into account. The EPC matrix elements are dependent on the electron wave vector as well and, therefore, $|g|^2$ is shown at $k = 0.218$ in figure 2.7, while in figure 2.8 at $k = 0.435$; these are the two points on the Fermi surface. In order to have a softening in the phonon mode (cfr. equation 1.16), there must be an intra- or inter-bands FSN and an EPC matrix element different from zero.

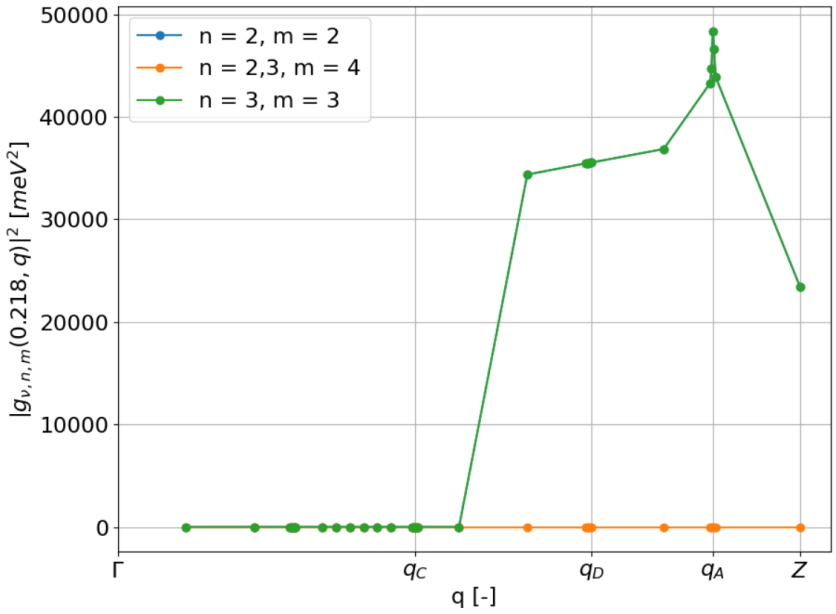

Figure 2.7: EPC matrix elements for the silicon NW on the longitudinal at $k = 0.218$. The line connecting the dots, here and in the following graphs representing EPC matrix elements, is just a guide to the eye.

Electronic bands are labelled with integers starting from 1 as the lowest energy band (cfr. figure 2.1 and appendix B). Therefore, at k_F^A bands 2 and 3 cross the Fermi energy, while at k_F^B only band 4 does. As a consequence, the possible FSNs are summarized in table 2.2. As it can be seen from the picture, the large dip at q_B on the longitudinal mode is due to the coupling between band 2 at wave vectors $-k_F^B$ and at k_F^B (the value of the matrix element is $\sim$ 53000 meV^2). Furthermore, the softening at q_A is due to the coupling of the phonon mode with intra-band transition between wave vector $-k_F^A$ and k_F^A of bands 3 (the values of the matrix element around the point are between 44000 and 48000 meV^2).

So far, the transverse mode has not been considered. The reason is

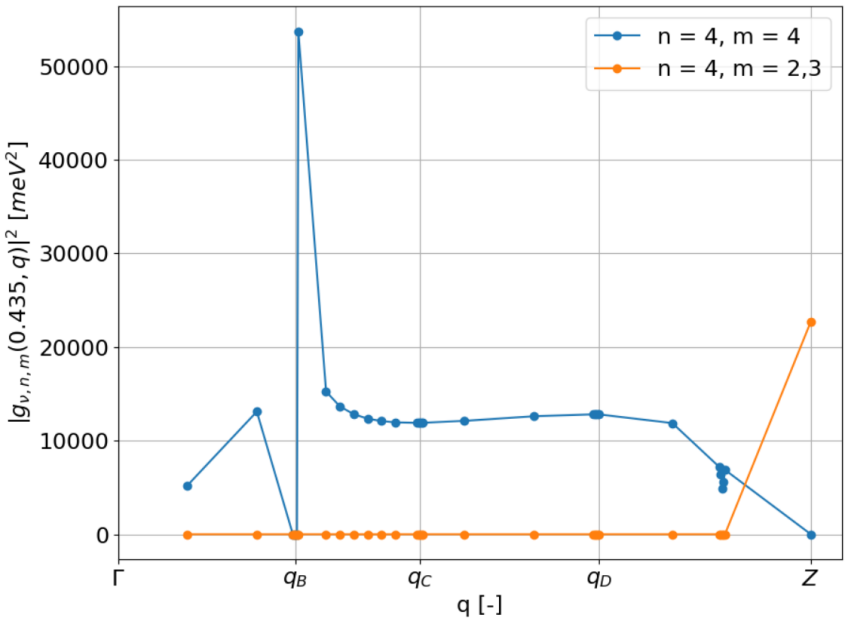

Figure 2.8: EPC matrix elements for the silicon NW on the longitudinal at $k = 0.435$.

k_F^A	q_A	q_B	q_C	q_D	k_F^B	q_A	q_B	q_C	q_D
$n = 2$, $m = 2$	YES	NO	NO	NO	$n = 2$, $m = 2$	NO	NO	NO	NO
$n = 2$, $m = 3$	YES	NO	NO	NO	$n = 2$, $m = 3$	NO	NO	NO	NO
$n = 3$, $m = 2$	YES	NO	NO	NO	$n = 3$, $m = 2$	NO	NO	NO	NO
$n = 3$, $m = 3$	YES	NO	NO	NO	$n = 3$, $m = 3$	NO	NO	NO	NO
$n = 2$, $m = 4$	NO	NO	YES	YES	$n = 2$, $m = 4$	NO	NO	NO	NO
$n = 3$, $m = 4$	NO	NO	YES	YES	$n = 3$, $m = 4$	NO	NO	NO	NO
$n = 4$, $m = 2$	NO	NO	NO	NO	$n = 4$, $m = 2$	NO	NO	YES	YES
$n = 4$, $m = 3$	NO	NO	NO	NO	$n = 4$, $m = 3$	NO	NO	YES	YES
$n = 4$, $m = 4$	NO	NO	NO	NO	$n = 4$, $m = 4$	NO	YES	NO	NO

Table 2.2: Summary of the possible FSNs at k_F^A (left-hand side of the table) and k_F^B (right-hand side).

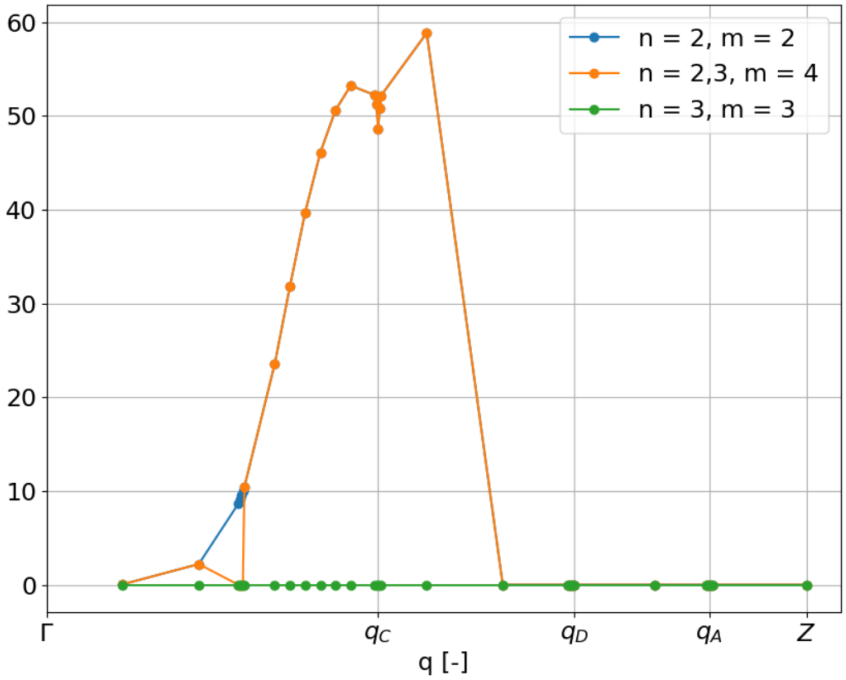

Figure 2.9: Modified EPC matrix elements for the transverse mode of silicon at k_F^A. The plotted values are the average of the two degenerate modes.

that, since this mode is unstable, the current treatment cannot be applied. As a matter of fact, in equation 2.14, it is clear that $|g|^2$ is defined only for positive frequencies and so the EPC matrix elements for the transverse mode cannot be computed. This is reasonable: it does not make much sense to investigate instabilities on a mode that is already unstable. However, since the softening of the mode can still be observed around q_C and q_D, it is interesting to calculate $|g|^2$ neglecting the term $1/\sqrt{\omega_{\nu,\vec{q}}}$. This will prevent the new calculated matrix elements from having any physical meaning, but it will still probe for the electron phonon coupling strength.

The results are shown in figures 2.9 and 2.10. As mentioned earlier, the new quantities are plotted for the two points of the Fermi surface. On the one hand, in figure 2.9, at the nesting between bands 2 and 3 at k_F^A and band 4 at k_F^B a finite matrix element is reported leading to a softening at q_C. On the other hand, nothing appreciable can be noticed at q_D for either points on the Fermi surface and for either bands. This is probably due to the fact that the softening is indeed really small and, therefore, the matrix element that leads to the softening is as small as the noise from the surrounding points.

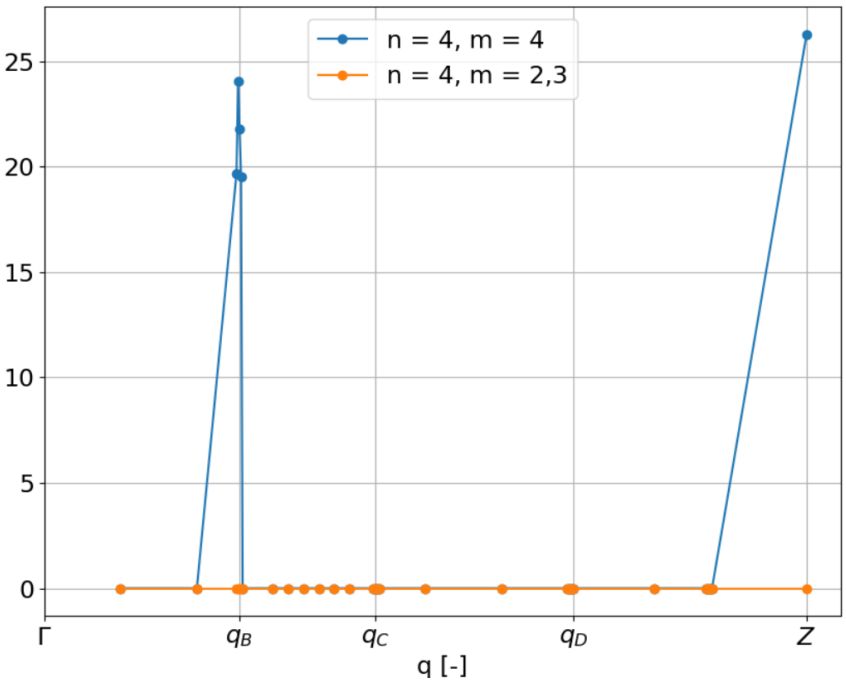

Figure 2.10: Modified EPC matrix elements for the transverse mode of silicon at k_F^B. The plotted values are the average of the two degenerate modes.

2.3.4 First-order perturbation of the potential

In this section, the interpolation of the first-order perturbation of the potential is explored. This will not add any physical results; however, since this kind of potentials is normally interpolated while computing EPC-related properties of materials, the effect of Kohn anomalies is interesting to be studied.

When dealing with electron-phonon interaction computation, $g_{\nu,n,m}$ on very dense q-grids are needed to be computed. Therefore, to lighten the computational costs of such calculation, it is possible to calculate the first-order perturbation potential at some points in the reciprocal space and then interpolate them with the FT scheme. An example of this is provided by the works of Brunin *et al.* [43, 44]. In figure 2.11, the imaginary part of $\Delta_{\vec{q},\nu} V^{KS}$ along the longitudinal mode is plotted. The choice of showing only this curve is made because this is the only meaningful result, while the others, i.e. real part of the longitudinal mode and both imaginary and real part of the transverse, give results close to zero. Moreover, it has to be mentioned that, at variance with the previous section, here there is no dependence the k-grid since the dependence on k appears in equation 2.13 when integrating with the wave function. The potential itself does not depend on k. The first-order perturbation of the

potential is averaged over the unit cell in real space.

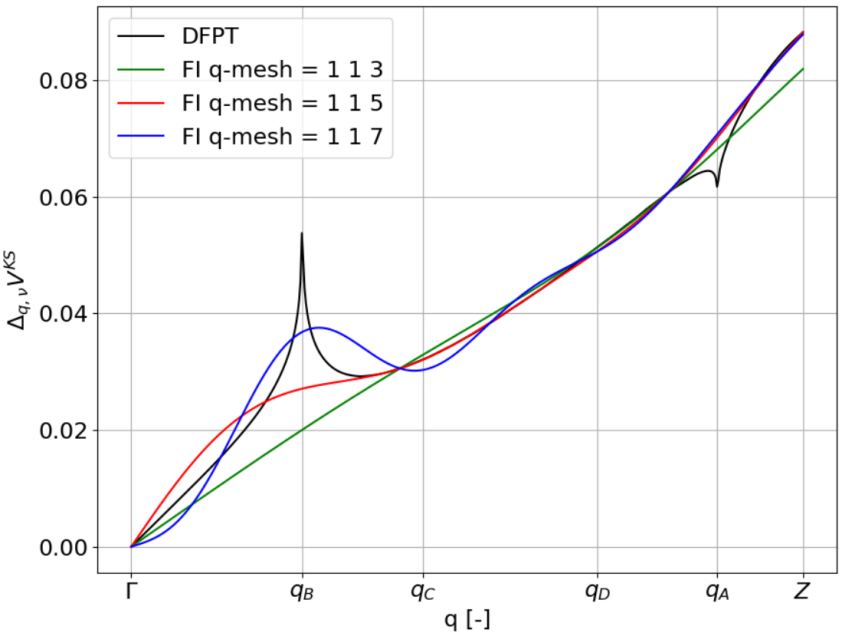

Figure 2.11: The imaginary part of the first-order perturbation of the potential in the longitudinal mode for silicon NW. The black line is DFPT-directly-calculated on a grid in the reciprocal space composed of five-hundred and one points. The green line is interpolated with FT scheme from a starting grid of three points. The same goes for red and blue for starting grids of five and seven points respectively.

On the one hand, from figure 2.11, it can be noted that around the two instabilities, the DFPT-calculated $\Delta_{\vec{q},\nu} V^{KS}$ shows non-analicity. This is a clear sign that the EPC matrix elements will show some divergence there (cfr. equation 2.13). On the other hand, it can be pointed out how the convergence of the interpolated curves is quite fast far from the instability. Indeed, at the center of the zone all the curves are superimposed. However, close to the anomalies the convergence is slow: no interpolated curve can reproduce the dip at q_A and the cusp at q_B is misrepresented.

In order to get an improvement, the quadrupolar interactions should be introduced in the computation, as it has been done in Ref. [43]. In the reference, long-range interactions induced by the incomplete screening of the potential generated by atomic displacement lead to non-analiticies at $q \to 0$. In metallic systems, these long-range interactions do not play a role, but the non-analicities are caused by the Kohn anomalies. Actually, the need of quadrupoles here is even stronger since in metallic systems there are no dipole-dipole interactions. Moreover, as already mentioned previously, an algorithm to predict the anomalies and incorporate them

into the interpolation is not available, but it would accelerate the convergence.

2.4 Zigzag silicon chain

As mentioned in section 2.3.2, the most stable configuration for the silicon chain should be the zigzag. Therefore, the steps for the linear chain are repeated for the zigzag one (cfr. figure 2.12). The starting structure is a two-atom unit cell. The bond length is the same as the starting one for the linear chain and the angle between the two bonds is of 125^o. The relaxed structure shows a bond length of 2.218 Å and an angle of 117^o.

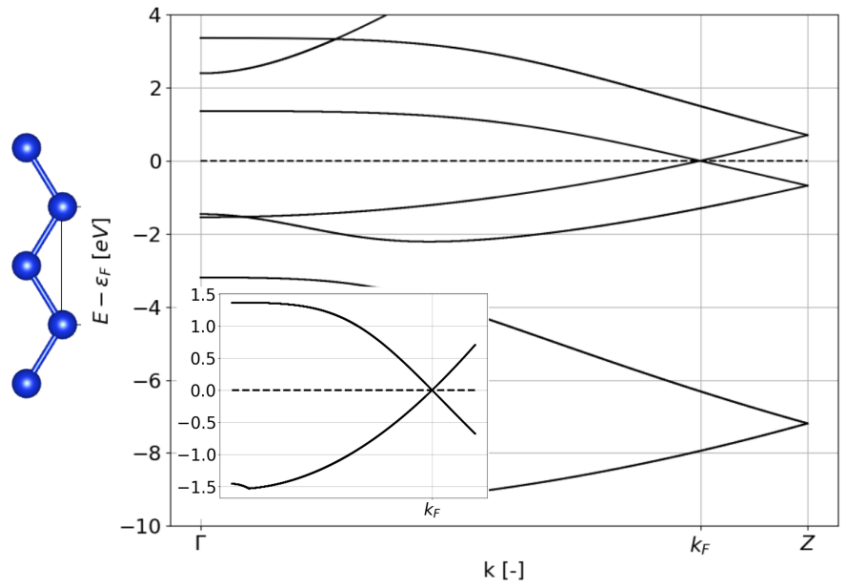

Figure 2.12: Zigzag silicon chain. On the left the structure is depicted, the bond length is 2.218 Å and the angle 117^o. On the right-hand side, the electronic band structure is depicted. The Fermi level is set to zero and it is represented as a dashed line. In the inset, a zoom around the Fermi surface is shown.

2.4.1 Electron band structure

In figure 2.12, the electron band structure is shown as well. Firstly, it can be noted that the zigzag structure is still metallic. The Fermi surface, as displayed in the inset, is composed of one point in the IBZ, $k = 0.4115$. As a consequence, a nesting will take place at $q_1 = 2 \times k_F = 0.177$. The point forming the FS is doubly degenerated.

2.4.2 Phonon band structure

In the structure, the two atoms per unit cell, each of which can be displaced in the three spacial directions, leads to six possible vibrational modes. The dispersion relation is shown in figure 2.13. Firstly, it can be noted that there is a Kohn anomaly in the most energetic optical mode and in the less energetic acoustic mode. The former appears at a temperature of 1×10^{-3} Ha (red curve), while it is cancelled at 1×10^{-2} Ha (black curve). The latter mode, being really close to zero, becomes negative. It might be a consequence of the Kohn anomaly and, therefore, a structural relaxation might take place. However, the shape of the instability is odd since it is relatively broad, but it still can be noted that there is clearly a dip close to q_1. This should be subject to further studies. Moreover, a final feature worth remarking is the mode which at 1×10^{-2} Ha is acoustic ($\omega \xrightarrow{q \to \Gamma} 0$), while at 1×10^{-3} Ha is characterized by a finite frequency. This should be studied further as well. It should be mentioned that the acoustic sum rule is imposed. The total energy should be invariant under translation of the crystal as a whole. This would guarantee that the three lowest phonon modes at Γ have zero frequency. However, since the IFCs are calculated on finite grids, the translational invariance might be slightly broken. As a consequence, a sum rule is imposed

$$\sum_{\kappa} \tilde{C}_{\kappa\alpha,\kappa'\alpha'}(\vec{q} = 0) = 0$$

where $\tilde{C}$ is the IFCs as defined in section 2.2.2.

2.5 Aluminum nanowires

Starting from the notions that have been discussed for the silicon NW, now the aluminum monoatomic chain will be studied and the results compared with the ones of the previous section. The two systems are quite similar, i.e. they are both linear monoatomic metallic chains, they just differ for one electron in the valence shell.

2.5.1 Electron band structure

The aluminum electron dispersion relation is portrayed in figure 2.14. The Fermi level has been brought to zero and it is depicted with a dashed line. There are just two points forming the Fermi surface in the 1BZ and, therefore, one in the IBZ at $k_F = 0.125$. As a consequence, a Kohn anomaly is expected to occur at $q = 2 \times k_F = 0.25$. The Fermi surface is double degenerate: bands 2 and 3 cross the Fermi level at k_F. Comparing

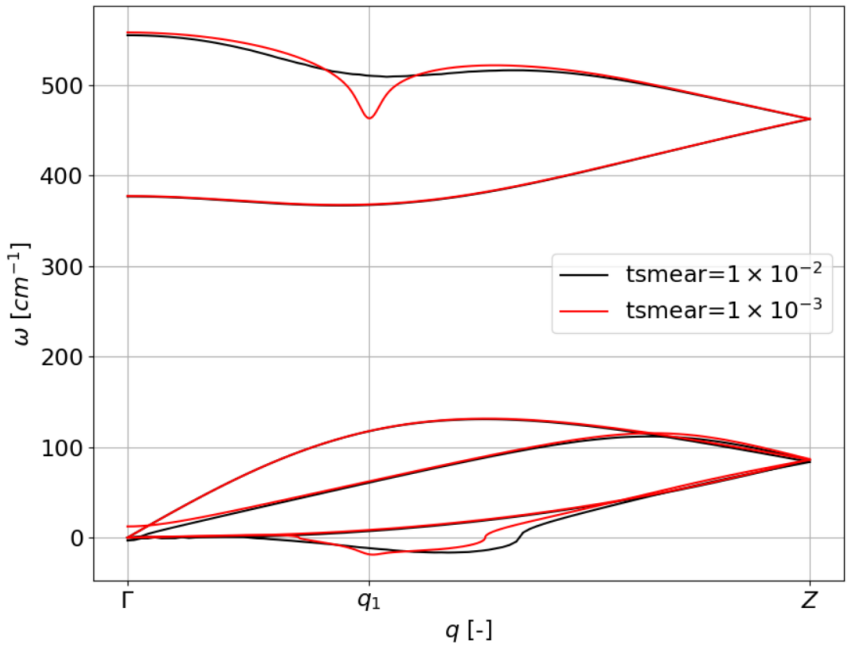

Figure 2.13: Phonon band structure for zigzag silicon chain. The dispersion relation is depicted for two temperature: 1×10^{-2} in black and 1×10^{-3} in red.

this result with the silicon's band structure it can be noted that they are indeed similar: the shape of the bands is the same. However, the Fermi energy is shifted at lower energy. Even though this is a little change, this shift has a big impact on the electronic properties: the Fermi surface, as mentioned, passes from two to one point and this leads to important consequences on the vibrational properties as well.

2.5.2 Phonon band structure

The phonon band structure is represented in figure 2.15. The dispersion relation shows again two modes, the longitudinal and the transverse. Since the softening of the transverse mode is small, the portrayed dispersion relation is at a temperature of 1×10^{-5} Ha; the used grid is composed of 201-equally-distanced points. In the inset, a zoom on the dip is shown. Even at such a low temperature the dip is of some cm^{-1} only. The position of the softening of the phonon mode is the one expected from the FSN. Contrarily to the case of silicon, the transverse mode here shows a Peierls instability at the zone's boundary.

Comparing this band structure with the one of silicon, it can be noted how the vibrational properties of metals are indeed difficult to predict. As a matter of fact, nevertheless the similarities, they show such different phonon dispersion relations. On the one hand, silicon shows an unstable

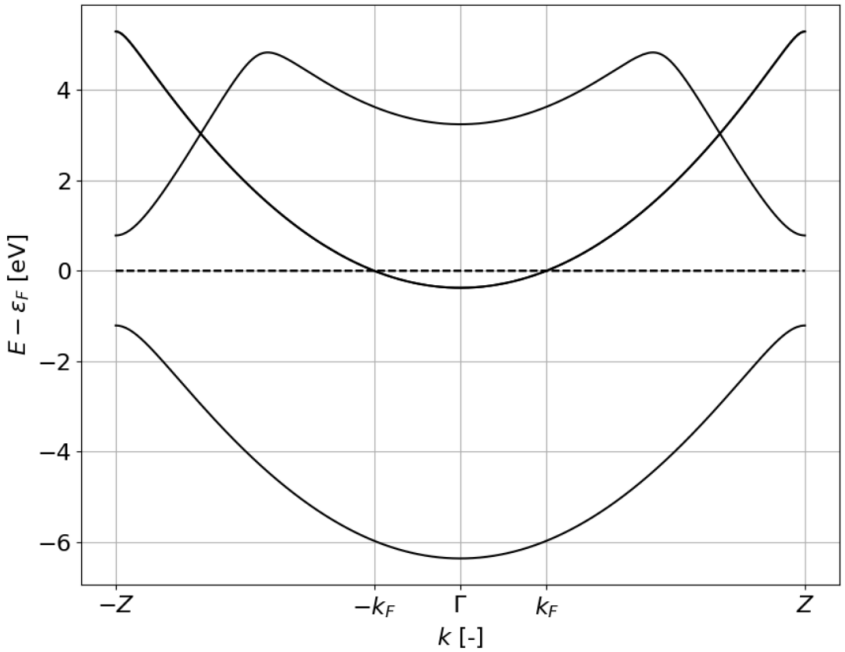

Figure 2.14: Electron band structure for aluminum nanowire. The Fermi level is set to zero and it is represented by a dashed line. The Fermi surface is indicated by the points $-k_F$ and k_F.

transverse mode, while the shape of the transverse mode of aluminum is totally different, with a Peierls instability at the zone boundary. On the other hand, the longitudinal mode, in the case of silicon, presents two large softenings corresponding to the two nesting vectors, one of them leading to an instability. Contrarily, for aluminum the softening is smaller in size and it is even misplaced. This, once again, calls for a need of a more general understanding of CDW in metals in order to obtain a systematic treatment of such systems.

2.5.3 EPC matrix elements & first-order perturbation of potential

In figures 2.16 and 2.17, EPC matrix elements for the two modes of aluminum around the FSN are shown. Once again, the portrayed quantities are $|g|^2$.

On the one hand, in figure 2.16, EPC matrix elements for the longitudinal mode are depicted. It can be noted how the values are all large and increasing with the q vector. At q the value is still large and the softening is due to the nesting between bands $n = 2$ and $m = 3$. On the other hand, in figure 2.17, the matrix elements for the transverse mode are shown. Even though there are large values even at the nesting

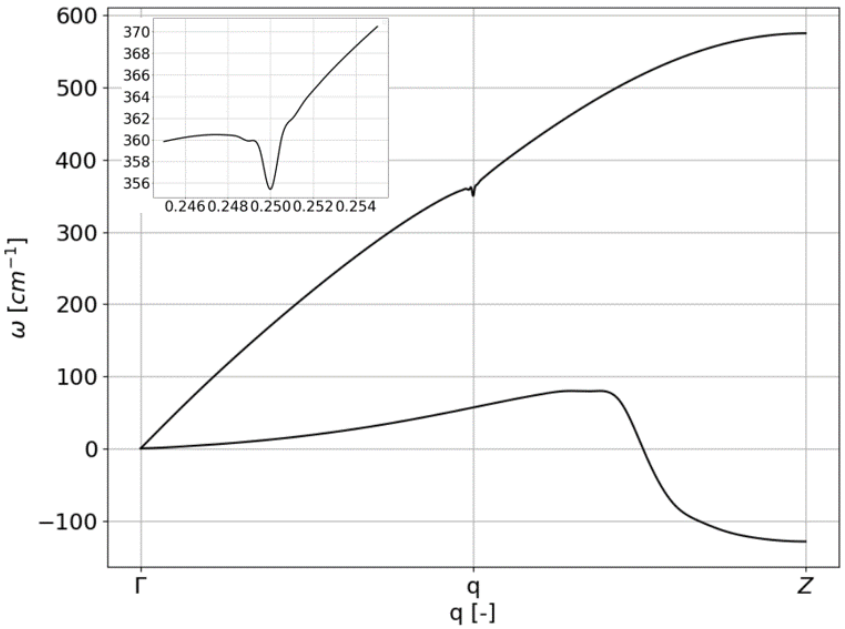

Figure 2.15: Phonon dispersion relation for an aluminum nanowire. The smearing temperature is 1×10^{-5} Ha, the q mesh is composed of 201-equally-distanced points. In the inset, a zoom around the softening of the mode is shown with the curve sampled with a grid composed by twice as many points.

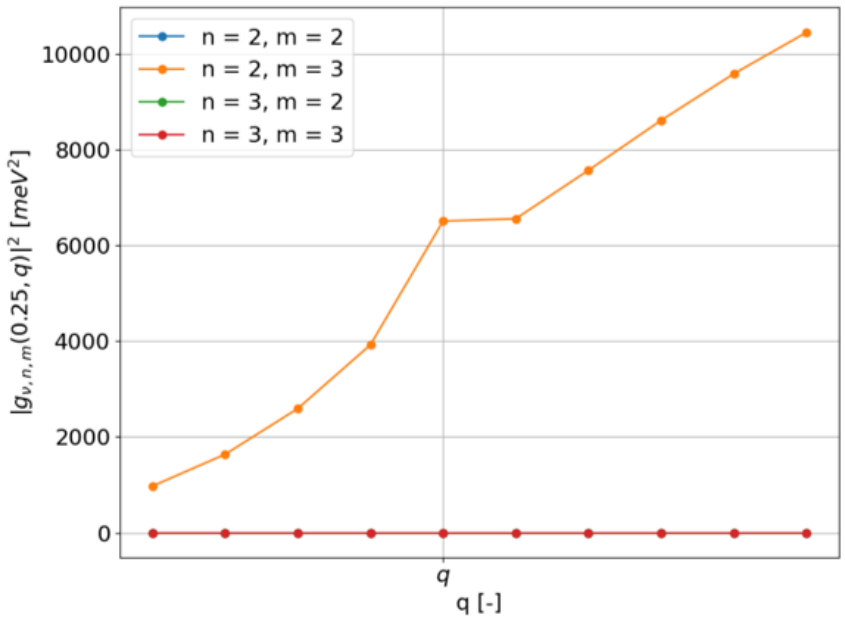

Figure 2.16: EPC matrix elements for longitudinal mode of aluminum nanowires around q.

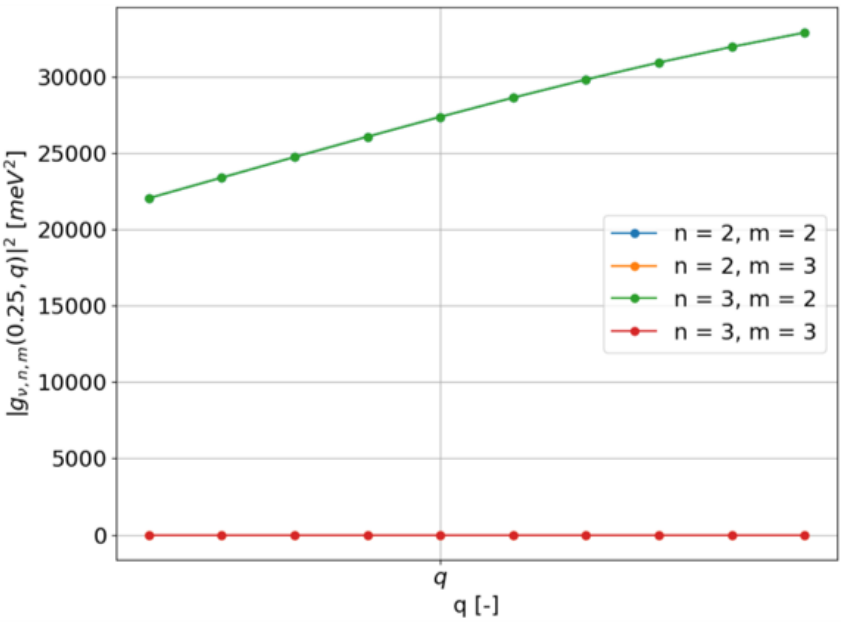

Figure 2.17: EPC matrix elements for transverse mode of aluminum nanowires around q.

vector, no dip is observed in the phonon dispersion relation. A possible explanation for this is that it is needed to include in the description of the phonon frequency higher order terms including in the picture other physical quantities, such as, for example, the Coulomb interaction (cfr section 1.6). However, this should be studied further.

In a similar fashion to what has been said for the first-order perturbation of potential for the silicon NW, also for aluminum the imaginary part of $\Delta_{\vec{q},\nu}V^{KS}$ for the longitudinal mode can be shown (figure 2.18).

As already discussed in the silicon case, close to the Fermi surface nesting $\Delta_{\vec{q},\nu}V^{KS}$ shows a non-analicity that is not represented by the FT interpolation. A conclusion similar to the one drawn in section 2.3.4 can be applied here as well.

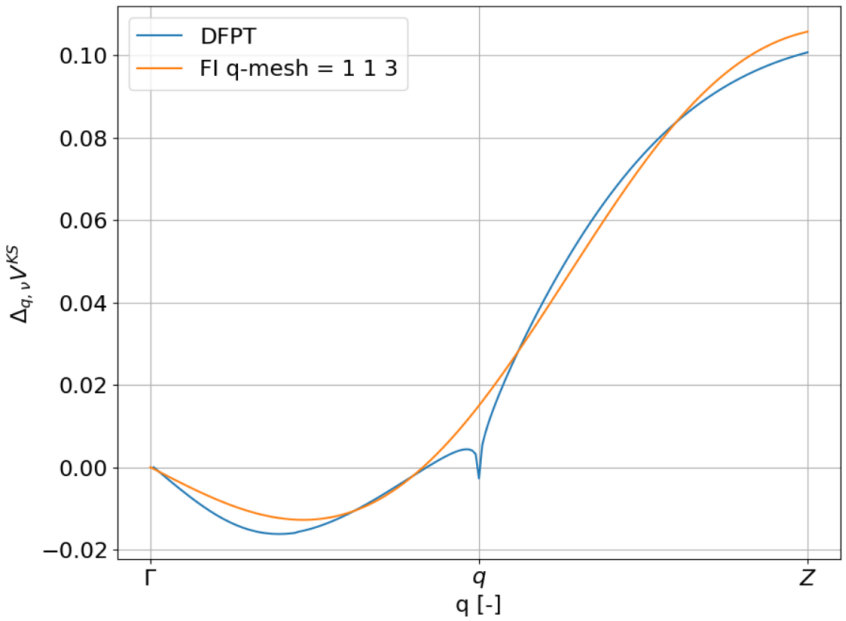

Figure 2.18: The imaginary part of the first-order perturbation of the potential in the longitudinal mode for aluminum NW. The blue line is DFPT-directly-calculated on a grid in the reciprocal space composed of two-hundred points. The orange line is interpolated with FT scheme from a starting grid of three points.

2.6 Bulk structures

As mentioned in the previous chapter, CDWs appear in 3D structures as well. In this section, some results on FCC silicon and aluminum are presented. The structure is composed by a single atom in the unit cell (cfr. figure 2.19). The space group is 225 ($Fm\bar{3}m$). However, the silicon FCC structure is not stable, it is studied as a system that shows Kohn anomalies. This bulk system becomes stable at high pressure [45].

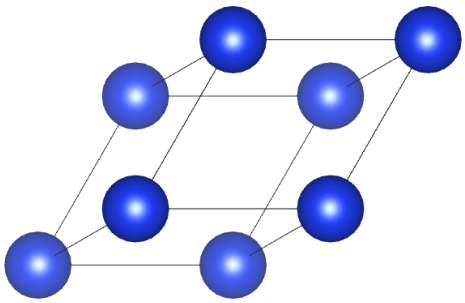

Figure 2.19: Unit cell of FCC bulk system.

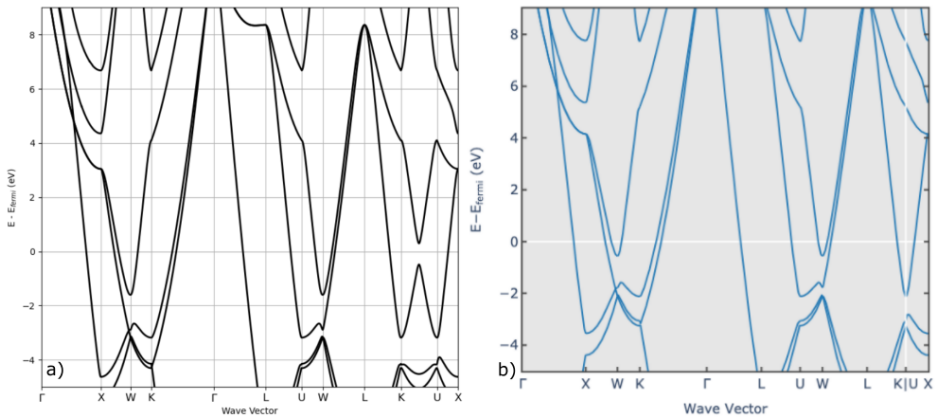

Figure 2.20: Electron band structure for silicon bulk. In panel a) the calculated dispersion relation is portrayed, while in panel b) the one from Material Project (mp-27).

Firstly, the lattice parameter has been relaxed for the two structures, starting from the cell dimensions taken from the Material Project [45]. The relaxed values are 3.87 Å for silicon and 4.03 Å for aluminum. All the calculations are carried out at a smearing temperature of 1×10^{-2} Ha.

2.6.1 Electron band structure

The electron band structures of the two systems are depicted in figures 2.20 and 2.21, where the calculated dispersion relations are presented next to the one from the Material Project.

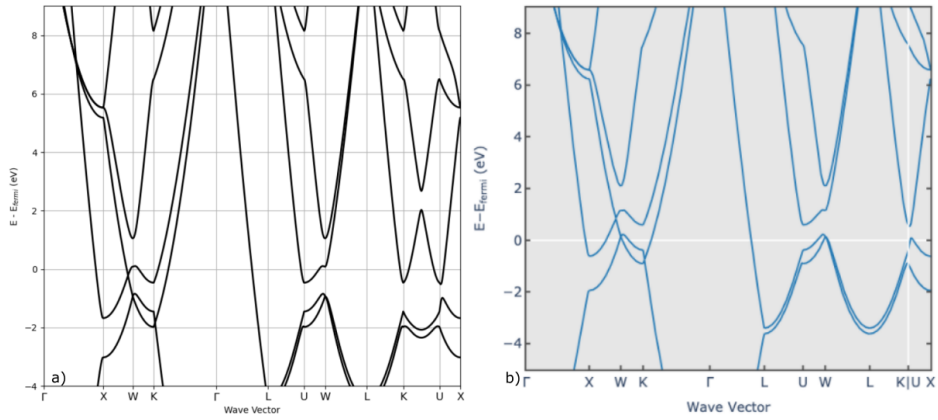

Figure 2.21: Electron band structure for aluminum bulk. In panel a) the calculated dispersion relation is portrayed, while in panel b) the one from Material Project (mp-134).

It can be noted that the two systems are metallic and that there is a good accordance between the calculated band structures and the ones from the reference. As for the linear chains, the shape of the dispersion relations of bulk silicon and aluminum are close one to the other. The main difference is the energy of the Fermi surface that is shifted. This is expected since the structure is the same and the two atomic species differ only for an electron in the valence shell. It is difficult to predict the appearance of CDWs in these cases since the nesting has not the big effect proven in one-dimensional chains. As it can be seen from figure 1.4 the origin of CDW in 3D materials does not lie in the divergence of Lindhard response function.

2.6.2 Phonon band structure

In this section, the phonon dispersion relations of the two systems are shown. As mentioned in section 2.3.2, high-throughput calculations for metallic phonon properties have not been carried out yet. This does not concern just linear chains or low-dimensional systems, but, in fact, all metals. Therefore, it is interesting to explore phonon dispersion relation of bulk metallic systems, to try to find some occurrence of CDWs and to investigate their possible origins.

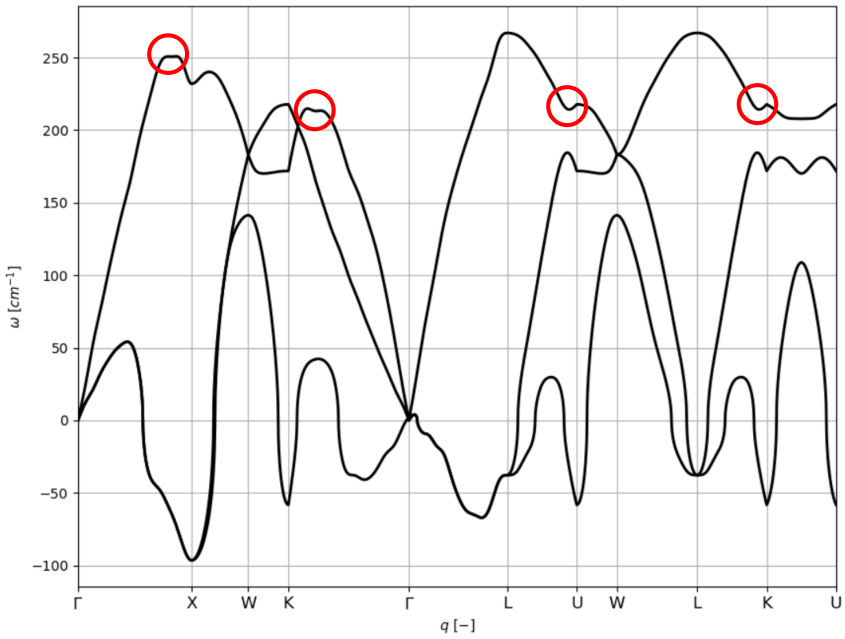

Figure 2.22: Phonon dispersion relation for FCC silicon.

In figure 2.22, the phonon dispersion relation of FCC silicon is plotted. From the figure, it can be noted that the FCC structure for the silicon

is not stable, i.e. there are some negative modes. It is well known that the stable configuration of bulk silicon is the diamond one. This unstable mode shows some peculiar oscillation around Γ, but these are the effect of the imposition of the acoustic sum rule.

Moreover, it can be noted that some modes soften, e.g. the most energetic mode close to K, U and X (marked with red circles in the figure). This might be due to Kohn anomalies.

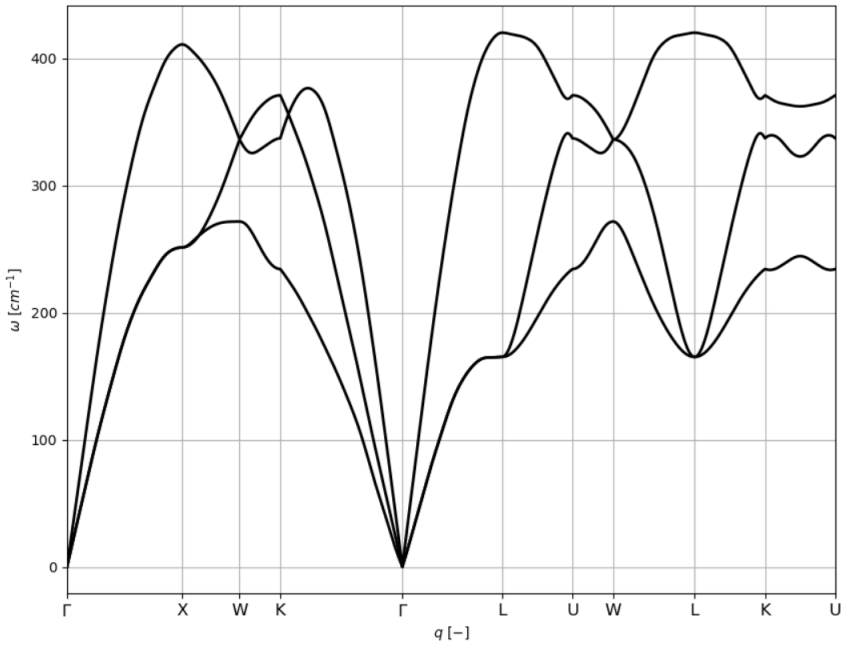

Figure 2.23: Phonon dispersion relation for FCC aluminum.

In figure 2.23 the phonon dispersion relation for FCC aluminum is portrayed. Firstly, it can be observed how this is the stable structure for the aluminum. As a matter of fact, no mode is unstable; however, similar features as the one highlighted in the case of silicon can be observed. Close to K and U, there are some softenings that can be related to a Kohn anomaly. Another dispersion relation has been calculated at a temperature of 5×10^{-3} Ha, but no differences have been observed. Further investigations on both systems should be performed.

2.7 Summary

In this chapter, the linear chains of silicon and aluminum together with the zigzag chain of silicon and the relative bulk systems have been studied. The appearance of CDWs in all these systems have been reported. In the case of the linear chain, the origin of these anomalies have been studied in more details since the situation is simpler and the appearance of Kohn anomalies is much clearer. In order to proceed, it is necessarily to better understand the origin of the instabilities in linear chain. Moreover, in order to improve the quality of the analysis for the 1D systems, on the one hand, more studies on the EPC matrix element of silicon zigzag chain should be carried out. On the other hand, the possible Peierls transition for the aluminum chain at the boundary zone should be examined. Furthermore, the bulk materials should be studied as well: firstly, investigating whether those indicated are in fact Kohn anomalies and then trying to find their possible origin, starting from the EPC. From this starting point, one can aim at a deeper understanding of the subject including also 2D materials (as mentioned in the introduction; see Ref. [4, 5] for some examples).

Conclusion

A charge density waves is the result of an instability of the electron gas that occurs in some metals below a transition temperature. Despite the fact that they have been known for almost a century now, a general understanding of the phenomenon is still lacking and this results in shortage of tools to treat metals in general. In this work, an attempt to better understand CDWs is made. In chapter 1, the theoretical background has been laid out. In particular, charge density waves have been introduced. After that, the theory of the Fermi surface nesting that leads to instability in the Lindhard response function has been explored. The two major consequences of this instability are Peierls transitions and Kohn anomalies. Details about the two physical phenomena have been described. On the one hand, the perturbation of the electronic density leads to a redistribution of the ions in the lattice: the unit cell doubles its size, doubling the number of atoms per unit cell as well. Moreover, the charge redistribution also has the consequence of opening a band gap at the boundary of the first Brillouin zone forcing the chain to undergo a metal-insulator transition. On the other hand, the CDW condensate, below a certain temperature, does not screen the virtual transition of the lattice anymore, leading to a softening of some phonon modes close to the nesting vectors. The amplitude of the softening, which is driven by the temperature, determines whether the lattice undergoes a relaxation or not. Afterwards, the role of electron-phonon coupling in the appearance of Kohn anomaly has been studied. The main result of the section is that the softening of a particular phonon mode is proportional to (i) $|g_{\nu,n,m}(\vec{k},\vec{q})|^2$ and (ii) the presence of a divergence in the real part of the Lindhard function.

In chapter 2, the results obtained from the first-principle calculations have been displayed. The computations have been carried out using the software Abinit and the Python-library Abipy (the used DFT and DFPT techniques have been reminded). The studied structures are silicon and aluminium monoatomic linear chains. In order to obtain the structures that minimize the energy, the chains have been relaxed. Afterwards, the electronic band structure has been computed. The shape of the dispersion relation is similar for both nanowires. The main difference is the

energy of the Fermi level, which in one case leads to a FS made of two points, while in the other only of one. The difference in the Fermi surface is reflected in the vibrational properties. As a matter of fact, only one FSN vector is expected for the IBZ of the aluminium chain, while for silicon the softening of the phonon mode is expected at four different q-points. Indeed, the phonon dispersion relation of silicon shows softenings of one mode for each nesting wave vector: in particular, the longitudinal mode has two large dips, one of which leads to an instability, while the transverse mode, which is unstable, shows two small dips at the other points. The fact that the unstable mode is the transverse one suggests that the most stable configuration of the silicon chain is the zigzag. This latter structure has also been studied. In order to build a zigzag chain, one has to use a unit cell with two atoms (the starting angle between the two bond is 125^o). The structure is relaxed as mentioned for the other systems and the electrical and vibrational properties are calculated. The chain is still metallic, and it still shows a region of instability. The band structure shows an instability close to the nesting vector due to the Kohn anomaly, which is anyway expected; the unforeseen fact is that the instability is quite broad. The aluminium chain displays a softening as well, but the amplitude is smaller even though the temperature is lower than the ones for silicon. Moreover, a Peierls instability occurs at the zone boundary. The analyzes of linear chains is continued with the computation of the electron-phonon matrix elements which, as reminded above, needs to be large enough in order to lead to a softening of the phonon mode. The two softenings for the longitudinal mode of silicon are due to the transition $-k_F^A \rightarrow k_F^A$ and to the transition $-k_F^B \rightarrow k_F^B$. Here, the fact that there are finite matrix elements in correspondence of nesting vectors that does not lead to a softening needs to be investigated further. As mentioned in the chapter, this can be due to the screening of the Coulomb interactions. For the transverse mode of silicon the instability at q_C is the result of the nesting between $k_F^A \rightarrow k_F^B$, while nothing appreciable can be noticed at q_D for either points on the Fermi surface and for either bands. Lastly, the phonon dispersion relations for the FCC silicon and aluminium have been computed.

From the computational point of view, different techniques to accelerate the computation of the phonon dispersion relation and the first order perturbation of the potential have been explored. The slow convergence of the curve representing these quantities is due to the Kohn anomalies and their unexpectedness. The lack of an algorithm that systematically predicts their appearances and their magnitude requires a large number of direct computations. In contrast, the interpolation on narrow grids leads to a misrepresentation of the physical quantities. For the phonon

band structure there is not a method to improve the quality of the interpolation without directly calculating more points in the IBZ. Instead, the computation's quality of the first-order perturbation of the potential may be enhanced by including quadrupoles interaction in the calculations. A clearer comprehension of the CDW phenomena as a whole is a key step in better understanding the behavior of metals. As a consequence, it will be possible to perform high-throughput calculations on metals as it is nowadays done with semiconductors.

Appendix A

Convergence studies

In Bloch theory, the wave function is described by a period function times a plane wave:

$$\phi_{n\vec{k}}(r) = u_{n\vec{k}}(\vec{r})e^{i\vec{k}\cdot\vec{r}} \tag{A.1}$$

The periodic coefficient can be expressed as

$$u_{n\vec{k}}(r) = \sum_{G} u_{n\vec{k}}(\vec{G})e^{i\vec{G}\cdot\vec{r}} \tag{A.2}$$

Therefore, the total wave function writes:

$$\phi_{n\vec{k}}(r) = \sum_{G} u_{n\vec{k}}(\vec{G})e^{i(\vec{G}+\vec{k})\cdot\vec{r}} \tag{A.3}$$

The coefficients for the lowest energy wave functions decrease exponentially with the kinetic energy $\frac{\vec{k}+\vec{G}}{2}$. The limit of the plane wave considered can be chosen using the energy cut-off.

$$\frac{\vec{k}+\vec{G}}{2} < E_{cut} \tag{A.4}$$

In principle, in order to have very accurate calculations, the largest number of plane waves should be included. However, filling the unit cell with several plane waves is computationally expensive and so a trade-off needs to be found. The other parameter, with respect to which a convergence is needed, is the number of points in the reciprocal space. On the one hand, the larger the number of sampling point, the more accurate is the computation; on the other hand, a too large number of points makes the calculation slower. Once again, a trade-off and a convergence study are needed. Both quantities are converged on the vacuum between the chains, the relaxed cell parameter, the electron energy and the phonon frequency. The convergence is always performed with a tolerance of the 0.2% with respect to the converged value.

In the following, all the convergence studies will be reported. In figure A.1, the convergence for the lattice parameter of the FCC aluminum, with respect to the cut-off energy and the number of k-points in the reciprocal space, is plotted as a proof of principles. The converged value is 4.033 Å. The convergence is quite fast and it is reached with a $10 \times 10 \times 10$ grid in reciprocal space and a cut-off energy of 12 Ha. As it will be seen, the requirements will become much stricter while converging other physical quantities. It is also interesting to compare the converged value of the cut-off energy with the values provided by the pseudo-dojo. As a matter of fact, the pseudopotentials provided are characterized by three values of cut-off energy: a low cut-off energy hint which is good for quick calculations, a normal cut-off energy hint for high-throughput calculations and a high cut-off energy hint beyond which no significant changes should be observed in the results. The value of the low energy hint for PBEsol ONCVPSP of aluminum is 16 Ha; however, it is well known that the convergence for metals is reached for low value of the cut-off energy.

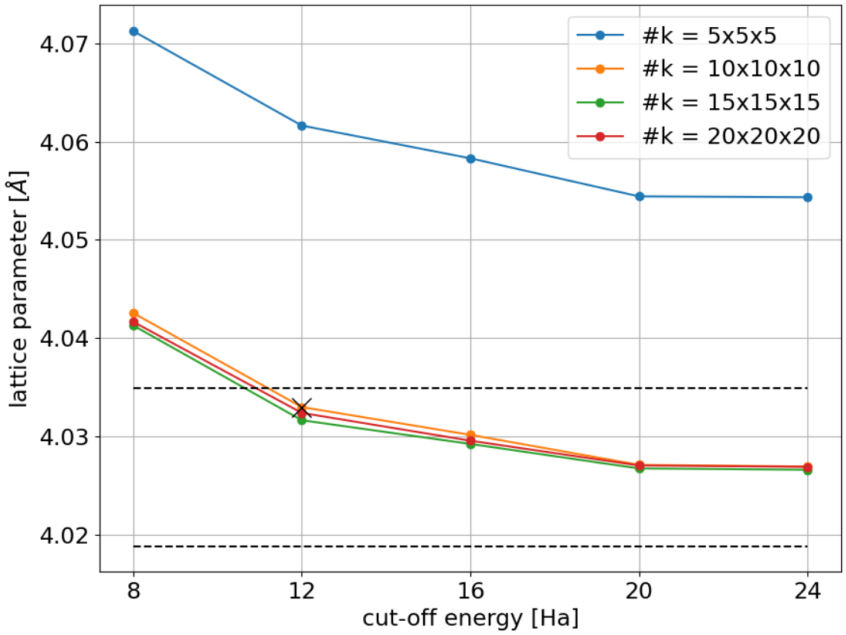

Figure A.1: Convergence study for the lattice parameter of the bulk aluminum with respect to the cut-off energy on the x-axis and the k-grid as a parameter. The tolerances are depicted by the black dashed line. A value is converged when it remains between the dashed lines. The converged value is marked with a cross.

In the following. the converged values will be reported without all the plots. The convergences for the monoatomic aluminum chain are displayed in table A.1.

Firstly, it needs to be remarked that converging the electron (phonon) band structure means to study the variation with respect to the number

Physical quantity	kpt [-]	ecut [Ha]
Bond length = 2.42 Å	10	8
Vacuum = 10 Å	10	12
Electron band structure	40	18
Phonon band structure at 0.01 - 0.0001 Ha	100	18
Phonon bandstructure at 1×10^{-5} Ha	4000	18

Table A.1: Summary of the convergence studies for the aluminum chain, kpt refers to the number of k-points in reciprocal space, while ecut to the cut-off energy.

of k-points and the cut-off energy of the electron energy (phonon frequency) at a certain point in reciprocal space. It can be noted that, in order to get a precise representation of band structures, the value of the cut-off energy needs to be in the order of the low hint value. It can be added that the bond length is also converged with respect to the smearing temperature: the converged value is 0.05 Ha.

In table A.2, the convergence study for the silicon chain is reported. The smearing temperature is converged again at 0.05 Ha for the bond length. The low hint for the cut-off energy of silicon is 14 Ha and all the convergences are quite close to this value.

Physical quantity	kpt [-]	ecut [Ha]
Bond length = 2.2 Å	40	10
Vacuum = 10 Å	40	10
Electron band structure	60	18
Phonon band structure at 1×10^{-2} Ha	100	10
Phonon bandstructure at 1×10^{-3} Ha	500	10
Phonon band structure at 1×10^{-4} Ha	3000	10

Table A.2: Summary of the convergence studies for the silicon chain.

The convergences of the silicon zigzag are presented in table A.3. The structure of the zigzag chain is composed of a unit cell with two atoms. The first one is place in position (0,0,0), while the position of the second needs to be relaxed together with the cell dimension along the wire axis. Since the dimension of the system in the direction perpendicular to the chain is increased, the cell dimension should be larger as well in order to keep the same vacuum between the NWs. The atomic positions are given in reduced coordinates (x_{red}) which provide the atomic position as a function of the real space primitive translations ($\vec{r}_{prim}$). These are typically numbers between 0 and 1 and the real space atomic coordinates are calculated as:

$$\vec{R} = x_{red}(1) \times \vec{r}_{prim}(1) + x_{red}(2) \times \vec{r}_{prim}(2) + x_{red}(3) \times \vec{r}_{prim}(3)$$

Physical quantity	kpt [-]	ecut [Ha]
Cell dimension = 3.78 Å	10	10
$x_{red}(1)$ = 0.103	30	10
Vacuum = 11 Å	30	10
Electron band structure	30	14
Phonon band structure at 1×10^{-2} Ha	250	14
Phonon bandstructure at 1×10^{-3} Ha	250	14

Table A.3: Summary of the convergence studies for the silicon zigzag chain. Xred refers to the reduced coordinate in the x direction of the second atom. The position in the y direction is zero and in the z direction is half of the unit cell.

For what concerns the bulks, the structural parameter that needs to converged is the dimension of the unit cell which is equal in the three directions, i.e. the same quantity converged in figure A.1. In table A.4, the convergences for the aluminum bulk is reported. It can be noted that the cut-off energy required for convergence is in the range provided by the pseudo-dojo. On the one hand, in order to have a good description of physical properties, a larger number of k-points is needed with respect to the linear chains, e.g. for the electron band structure the bulk needs $15 \times 15 \times 15 = 3375$ points, while the aluminum linear chain needs only $1 \times 1 \times 40 = 40$ points. On the other hand, the cut-off energy is similar in the two cases.

Physical quantity	kpt [-]	ecut [Ha]
Lattice parameter = 4.033 Å	$10 \times 10 \times 10$	12
Electron band structure	$15 \times 15 \times 15$	20
Phonon band structure at 1×10^{-2} Ha	$20 \times 20 \times 20$	20
Phonon band structure at 5×10^{-3} Ha	$25 \times 25 \times 25$	20

Table A.4: Summary of the convergence studies for the bulk aluminum.

Lastly, the convergence studies for the FCC silicon are reported in table A.5. As it was noted for the linear chain, the needed cut-off energy for silicon is generally lower than the one for aluminum. It can also be noted that in order to get a good representation of the band structures for the bulks the E_{cut} needs to be in the range of the normal hint.

Physical quantity	kpt [-]	ecut [Ha]
Lattice parameter = 3.875 Å	$15 \times 15 \times 15$	10
Electron band structure	$15 \times 15 \times 15$	10
Phonon band structure at 1×10^{-2} Ha	$40 \times 40 \times 40$	18

Table A.5: Summary of the convergence studies for the bulk silicon.

Appendix B

Electronic band structures

In this section, the different electronic bands for the silicon and aluminum monoatomic chain are presented. Figure B.1 represents the first four bands of silicon, from the first a) to the fourth d). It can be noted that, as mentioned in section 2.3.3, the Fermi surface is composed by the points k_F^A, where bands 2 and 3 cross the Fermi level, and k_F^B, where just band 2 crosses the Fermi level. As a consequence, the possible nestings are the ones summarized is table 2.2.

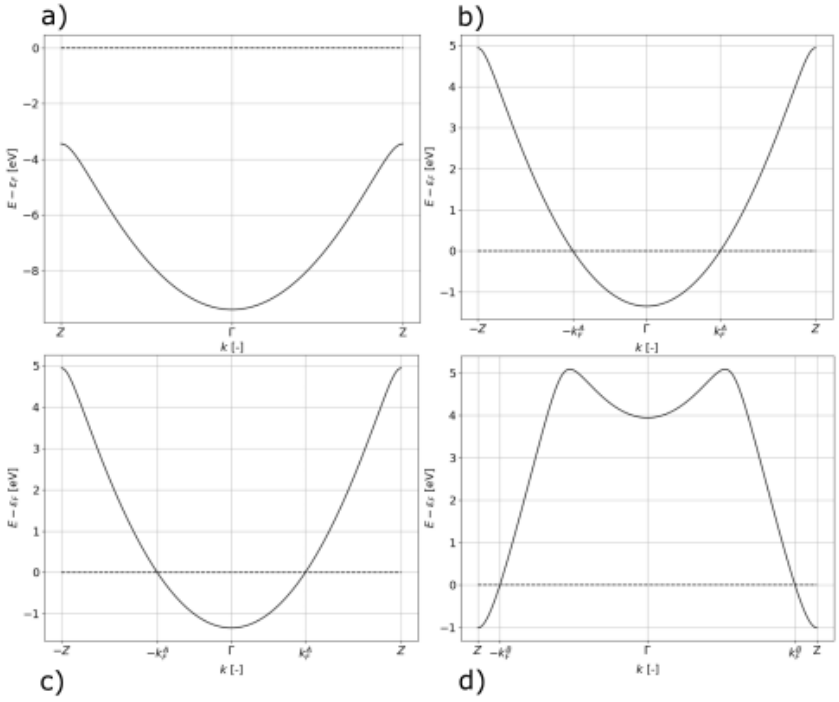

Figure B.1: Electronic bands of silicon monoatomic chain. In panel a) band 1 is represented, in b) 2, c) 3 and d) 4. The Fermi level is represented in all the plots with a dashed line.

The same is shown for the aluminum monoatomic chain. The results are portrayed in figure B.2. As already mentioned, the Fermi surface is composed of a point in the IBZ, which is doubly degenerated (bands 2 and 3). Therefore, the four possible nestings are $-k_F^2 \rightarrow k_F^2$, $-k_F^2 \rightarrow k_F^3$, $-k_F^3 \rightarrow k_F^2$ and $-k_F^3 \rightarrow k_F^3$, where the superscripts are the electronic bands.

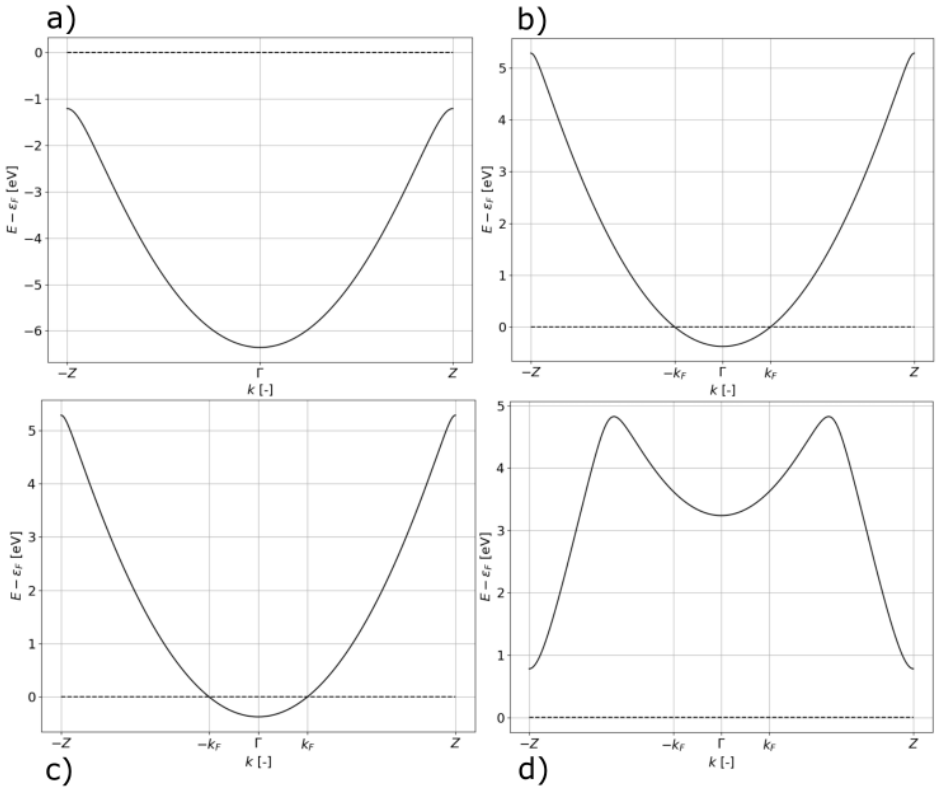

Figure B.2: Electronic bands of aluminum monoatomic chain. In panel a) band 1 is represented, in b) 2, c) 3 and d) 4. The Fermi level is represented in all the plots with a dashed line.

A final comment on the electronic band structure of the FCC system is needed. Looking at the comparison between calculated electron band structures and the reference (cfr. figures 2.21 and 2.20), it can be noted that a small shift in energy is present. However, these small shifts have a little impact since the bands are very dispersive, i.e. the slope of the bands is large. This fact is confirmed also analyzing the Density of States (DOS). The DOS of the bulk aluminum is reported in figure B.3. The Fermi level is set to 0 eV. It can be noted that, even slightly changing the electron energy, the DOS around the Fermi level changes a little. Therefore, the effect of the shift reported in the figures of chapter 2 is negligible.

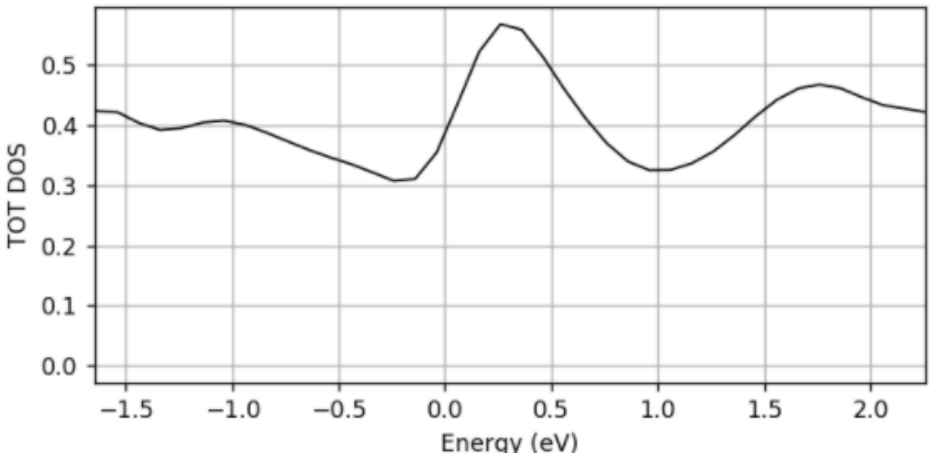

Figure B.3: Total DOS for the bulk aluminum around the Fermi level, which is set to zero.

Bibliography

[1] "The dynamics of charge-density waves", Grüner G., *Reviews of Modern Physics*, **60**, 4 (1988)

[2] "Zur Theorie der elektrischen und thermischen Leitfähigkeit von Metallen", Peierls R., *Annalen der Physik*, **396**, 122-148 (1930)

[3] "Theory for the Charge-Density-Wave Mechanism of 3D Quantum Hall Effect", Qin F., Li S., Du Z.Z., et al., *Physical Review Letters*, **125**, 206601 (2020)

[4] "Van der Waals driven anharmonic melting of the 3D charge density wave in VSe2", Diego J., Said A. H., Mahatha S. K., *Nature Communications*, **12**, 598 (2021)

[5] "Theory of the thickness dependence of the charge density wave transition in 1 T-TiTe2", Zhou J.S., Bianco R., Monacelli L., *2D Materials*, **7**, 045032 (2020)

[6] "Misconceptions associated with the origin of charge density waves", Zhu X., Guo J., Zhang J., et al., *Advances in Physics: X*, **2:3**, 622-640 (2017)

[7] "The Abinit project: impact, environment and recent developments", Gonze X., Amadon B., Antonius G., et al., *Computer Physics Communications*, **248**, 107042 (2020)

[8] "ABINIT: Overview, and focus on selected capabilities",Romero A.H., Allan D.C., Amadon B., et al., *The Journal of Chemical Physics*, **152**, 124102 (2020)

[9] "Recent developments in the ABINIT software package",Gonze X., Jollet F., Araujo F.A., et al., *Computer Physics Communications*, **205**, 106-131 (2016)

[10] "ABINIT: First-principles approach to material and nanosystem properties",Gonze X., Amadon B., Anglade P.M., et al., *Computer Physics Communications*, **180**, 2582-2615 (2009)

[11] "A brief introduction to the ABINIT software package", Gonze X., Rignanese G.M., Verstraete M., et al., *Zeitschrift für Kristallographie - Crystalline Materials*, **220**, 558-562 (2005)

[12] "First-principles computation of material properties: The ABINIT software project", Gonze X., Beuken J.M., Caracas R., *Computational Materials Science*, **25**, 478-492 (2002)

[13] "Abipy overview", url: http://abinit.github.io/abipy/features.html (July 7, 2021)

[14] "Image of the Fermi surface in the vibration spectrum of a metal", Kohn W., *Physical Review Letters*, **2**, 393-394 (1959)

[15] "Extended Phonon Collapse and the Origin of the Charge-Density Wave in 2H-NbSe2", Weber F., Rosenkranz S., Castellan J.P., et al., *Physical Review Letters*, **107**, 107403 (2001)

[16] "Density Waves in Solids", Grüner G., *Addison-Wesley Publishing Company* (1994)

[17] "First-principles investigation of monatomic gold wires under tension", He L., Liu F., Li J., et al., *Computational Materials Science*, **171**, 109226 (2020)

[18] "Classification of charge density waves based on their nature", Zhu X., Cao Y., Zhang J., et al., *Proceedings of the National Academy of Science*, **112**, 8 (2015)

[19] "Fermi surface nesting and the origin of charge density waves in metals", Johannes M.D., Mazin I.I., *Physical Review B*, **77**, 165135 (2008)

[20] "Electron-phonon interactions from first principles", Giustino F., *Reviews of Modern Physics*, **89**, 1539-0756 (2017)

[21] "Electron-phonon interaction in ultrasmall-radius carbon nanotubes", Barnett R., Demler E. and Kaxiras E., *Physical Review B*, **71**, 035429 (2005)

[22] "Quasi-One-Dimensional Fermi Surface Nesting and Hidden Nesting Enable Multiple Kohn Anomalies in α-Uranium", Roy A.P., Bajaj N., Mittal R. et al., *Physical Review Letters*, **126**, 096401 (2021)

[23] "Notes", Li J. (12-09-2012)

[24] "Notes", Rignanese G.-M. (12-08-2020)

[25] "Electrical Transport Properties in $2-HNbS_2, -NbSe_2, -TaS_2 and Ta_Se_2$", Naito M., Tanaka S., *Journal of the Physical Society of Japan*, **51**, 1 (1982)

[26] "Quasiparticle Spectra, Charge-Density Waves, Superconductivity, and Electron-Phonon Coupling in $2H - NbSe_2$", Valla T., Fedorov A.V., Johnson P.D., *Physical Review Letters*, **92**, 8 (2004)

[27] "Generalized Gradient Approximation Made Simple", Perdew J.P., Burke K., Ernzerhof M., *Physical Reviews Letters*, **77**, 3865-3868 (1996)

[28] "Optimized norm-conserving Vanderbilt pseudopotentials", Hamann D.R., *Physical Review B*, **88**, 085117 (2013)

[29] "The PseudoDojo: Training and grading a 85 element optimized norm-conserving pseudopotential table", van Setten M.J., Giantomassi M., Bousquet E. et al., *Computer Physics Communications*, **226**, 39-54 (2018)

[30] "LMAPR2451 - Atomistic and nanoscopic simulations", Rignanese G-M, Charlier J.C., Gonze X. (2020)

[31] "Inhomogeneous Electrons Gas", Hohenberg P., Kohn W., *Physical Review*, **136**, 136 (1964)

[32] "Self-Consistent Equations Including Exchange and Correlation Effects",Kohn W., Sham L. J., *Physical Review*, **140**, 4A (1965)

[33] "Dynamical matrices, Born effective charges, dielectric permittivity tensors, and interatomic force constants from density-functional perturbation theory", Gonze X., Lee C., *Physical Review B*, **55**, 10355 (1997)

[34] "Ab initio calculation of the thermodynamic properties and atomic temperature factors of $SiO_2 \alpha$-quartz and stishovite", Lee C., Gonze X., *Physical Review B*, **51**, 8610-8613 (1995)

[35] "Phonons and related crystal properties from density-functional perturbation theory", Baroni S., de Gironcoli S., Dal Corso A., et al., *Reviews of Modern Physics*, **73**, 515 (2001)

[36] "Density-functional approach to nonlinear-response coefficients of solids", Gonze X., Vigneron J.-P., *Physical Review B*, **39**, 13120 (1989)

[37] "Adiabatic density-functional perturbation theory", Gonze X., *Physical Review A*, **52**, 1096 (1995)

[38] "First-principles responses of solids to atomic displacements and homogeneous electric fields: Implementation of a conjugate-gradient algorithm", Gonze X., *Physical Review B*, **55**, 10337 (1997)

[39] "Many-body perturbation theory approach to the electron-phonon interaction with density-functional theory as a starting point", Marini A., Ponc S., Gonze X., *Physical Review B*, **91**, 224310 (2015)

[40] "Introduction to Quantum Mechanics", Griffiths D. J., *Cambridge: Cambridge University Press* (2017)

[41] "Convergence and pitfalls of density functional perturbation theory phonons calculations from a high-throughput perspective", Petretto G., Gonze X., Hautier G. et al., *Computational Materials Science*, **144**, 331-337 (2018)

[42] "High-throughput density-functional perturbation theory phonons for inorganic materials", Petretto G., Dwaraknath S., Miranda H.P.C. et al., *Scientific Data*, **5**, 180065 (2018)

[43] "Electron-Phonon beyond Fröhlich: Dynamical Quadrupoles in Polar and Covalent Solids", Brunin G., Miranda H-P-C, Giantomassi M., et al., *Physical Review Letters*, **125**, 136601 (2020)

[44] "Phonon-limited electron mobility in Si, GaAs, and GaP with exact treatment of dynamical quadrupoles", Brunin G., Miranda H-P-C, Giantomassi M., et al., *Physical Review B*, **102**, 094308 (2020)

[45] "The Materials Project: A materials genome approach to accelerating materials innovation", Jain A., Ong S.P., Hautier G., *APL Materials*, **1**, 011002 (2013)

[46] "Special points for Brillouin-zone integrations", Monkhorst H. J., Pack J.D., *Physical Review B*, **13**, 12 (1976)

[47] "Solid State Physics", Ashcroft, Mermin, *Cengage* (1975)